AN ABSTRACT OF THE THESIS OF

Fanghui Ren for the degree of Doctor of Philosophy in Electrical and Computer Engineering presented on November 16, 2016.

Title: Surface-Normal Modulation of Fano Resonances in Metallic Photonic Crystals for Free-Space Optical Interconnects.

Abstract approved:

_____

Alan X. Wang

This dissertation focuses on the development of ultra-compact optical devices for free-space modulation. We propose a surface-normal modulator using metallic photonic crystals for free-space optical interconnects. The active control of light intensity is achieved by engineering the Fano resonances in metallic photonic crystals. Both thermo-optic modulation and electro-optic modulation of the plasmonic bandgap are investigated, and bandgap tuning due to those effects is demonstrated. Additionally, the potential application of Fano resonances in metallic photonic crystals can be found in all-optical switching processing devices. Therefore, we show a hybrid plasmonic-organic nanostructure with extraordinary third harmonic generation emission at 1550 nm. Lastly, a simple method is proposed in this work to investigate the effect of finite grating size on Rayleigh anomaly-surface plasmon polariton (RA-SPP) resonances. The model could quickly and effectively predict the broadening of the transitional edges of RA-SPP resonances, which agrees well with experimental results quantitatively.

Surface-Normal Modulation of Fano Resonances in Metallic Photonic Crystals for Free-Space Optical Interconnects

by
Fanghui Ren

A THESIS

submitted to

Oregon State University

in partial fulfillment of
the requirements for the
degree of

Doctor of Philosophy

Presented November 16, 2016
Commencement June 2017

Doctor of Philosophy thesis of Fanghui Ren presented on November 16, 2016

APPROVED:

Major Professor, representing Electrical and Computer Engineering

Director of the School of Electrical Engineering and Computer Science

Dean of the Graduate School

I understand that my thesis will become part of the permanent collection of Oregon State University libraries. My signature below authorizes release of my thesis to any reader upon request.

Fanghui Ren, Author

ACKNOWLEDGEMENTS

I would like to express my appreciation to my advisor Professor Alan X. Wang for the guidance and advising through my graduate education. It was only because of his keen interest and careful supervision that gave my work this extent form. My appreciation also extends to Professor John Conley, Professor Huaping liu, Professor Larry Cheng, and Professor Maggie Niess for serving as my committee members.

I also would like to thank all my current and former laboratory colleagues for their academic support and friendship. They are Qian Gao, Xinyuan Chong, Erwen Li, Jing Yang, Xianming Kong, Spencer Liverman and Xiangyu Wang. I am also very fortunate to work with many bright colleagues in the materials and devices groups at EECS department in Oregon State University. I am very grateful that Rick Presley and Chris tasker provided me a lot of guidance through my study.

I want to specially thank Dr. Kevin Cai for his mentoring when I worked as an intern at Cisco. It has been a great enriching experience to me to work under his guidance.

Finally, I would like to acknowledge with gratitude, the support and love of my parents. The completion of my Ph.D study would not have been possible without them.

TABLE OF CONTENTS

Page

TABLE OF CONTENTS (Continued)

Page

LIST OF FIGURES

Figure Page

Surface-Normal Modulation of Fano Resonances in Metallic Photonic Crystals for Free-space Optical Interconnects

CHAPTER 1. INTRODUCTION

The world's technological capacities to store, communicate, and compute information are quickly growing at exponential rates. Optical fiber has already taken over the task of long-haul communications from electrical wires and has also been widely used in connections between different parts of large electronic systems [1-4]. Recent research efforts have focused on using optical interconnects for short-distance communication, which have several advantages compared to traditional copper interconnects. Optical interconnects can offer decreased interconnect delays and provide a large transmission bandwidth. Additionally, optical interconnects require lower power consumption and are inherently immune to electromagnetic interference [5-8].

In general, short interconnects can be divided into the following categories: rack-to-rack (a few meters to 100s of meters), inter-shelf or possibly on large boards or backplanes (a few cm to a few meters), chip-to-chip (a few cm) and on-chip interconnects (up to a few cm). Figure 1.1 summarizes optical interconnects at different levels. Industrial products on board-level have been rising stars in the market but chip-level interconnects are still in research stages. There is a wide range of research investigating different material systems and architectures for on-chip optical interconnects, however the practicality and the feasibility using optics for on-chip optical interconnects is still an open question [9-10].

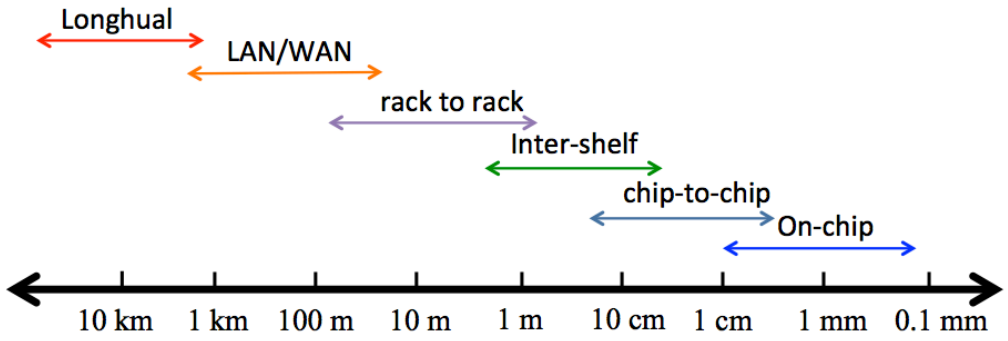

Figure 1.1: The coverage of optical communication at different levels.

Fibers have already been used for system interconnects and backplanes, however, the demand for bandwidth growth and high integration density has led us to move the design from waveguide to free-space interconnection. In recent two decades, significant progress has been made in enabling technologies for free-space optical interconnects for digital systems, including the hybrid integration of vertical cavity surface emitting lasers (VCSELs) with silicon integrated circuits [11-16]. Such technology is expected to be capable of providing high bandwidth communication links both within and between high-performance electronic systems.

Although existing photonic technologies using directly modulated VCSELs have readily enabled parallel or 3-D optical interconnects [17-19], external modulation offers several advantages. The operation of the light source does not need to be compromised by direct modulation. The power budget is much lower

as the single light source can be directed into multiple channels using individual modulators. In free-space optical links, external modulation using an optical modulator is expected to achieve efficient and high bandwidth data transmission. This dissertation focuses on the development of ultra-compact optical devices for free-space modulation. There is a wide range of research investigating different materials and device structures for optical modulators. Among the material and device choices, plasmonics is our interest for ultra-efficient and high bandwidth modulators.

In this chapter, the advantages of free-space optical interconnects over waveguide links will be discussed. We will then discuss motivation for developing a surface-normal modulator in a free-space optical link. Challenges for surface-normal modulation and the motivation for designing a plasmonic modulator will also be discussed in this chapter.

1.1. Free-Space Optical Interconnects

As mentioned above, optical interconnections have been of interest at all levels in communication systems for applications between mainframes, modules, boards, chips, and now within a chip. Our primary interest is optical devices for free-space optical modulation, which could be applied for short-distance communications aimed at high performance electronic systems, as copper interconnections between electronic cards via PCB backplanes become a

bottleneck in high-end systems such as servers, telecom switches, and advanced radar systems.

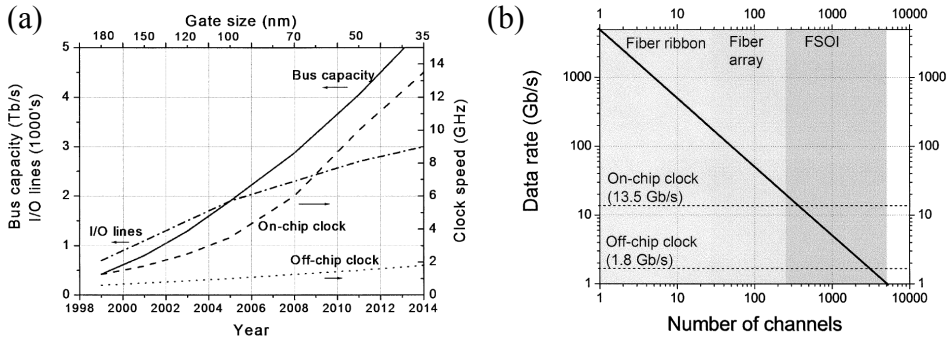

Figure 1.2: (a) Increase in on-chip & off-chip clock speed, high-speed off-chip clock lines and I/O capacity during the past two decades; (b) Free-space optical interconnects have much higher channel density with large data rate, reprinted with permission from [21].

Figure 1.2(a) shows increase in on-chip clock speed, off-chip clock speed, number of high-speed off-chip clock lines and total off-chip I/O capacity as a function of years in VLSI transistors for high-performance systems [21]. It can be seen that at 35 nm gate size, the off-chip clock speed reaches 1.8 GHz and the width of the off-chip bus also increases to 3000 high-speed lines, with a total estimated off-chip I/O capacity of 5 Tb/s. Figure 1.2(b) plots the data rate per channel required to achieve 5 Tb/s as a function of parallel channel numbers without considering serialization/deserialization circuits, taken from [21]. The shaded different regions correspond to optical interconnect formats in fiber ribbon,

fiber arrays and free-space optical interconnects, respectively. It can be clearly seen that compared to fiber-array solutions, free-space optical interconnect solutions allow much more channels. Such dense integration has been experimentally demonstrated by using a 512-channel inter-chip interconnects with array density 28 channels/mm. [22].

Free-space optical interconnects taking advantages of 2-D array of VCSELs have been developed and investigated [17-19, 22]. A VCSEL is a nanoscale heterostructure with several-micron footprint emitting a highly efficient optical beam vertically from its top surface. A VCSEL consists of an InGaAs quantum well active region with a PN junction structure for carrier injection, a top and bottom distributed Bragg reflectors as a resonant cavity, which are fabricated on a GaAs substrate using molecular beam epitaxy (MBE) or metal-organic chemical vapor deposition (MOCVD). An attractive feature of VCSELs is their capability of being fabricated into uniform, individually addressable 1D or 2-D arrays, which could provide light emission without the need of external laser sources and pre-routing those laser sources. VCSELs, modulators, photodetectors (PDs) and collimating microlens can be implemented with standard III-V semiconductor technologies, and 3-D integrated with CMOS based transmitter and receiver electronics.

Optical backplanes could be one of the applications utilizing optical signals to realize communications could potentially meet the data-rate requirement for the high-performance computing systems [23-25]. Current optical interconnects

mainly use waveguided interconnections, which consists multiple waveguides or fibers between communicating components. Polymer waveguides on PCBs and waveguide bus architectures are the mostly developed technologies for in-plane point-to-point and broadcasting optical interconnects [23-25]. Efforts in improving performance of backplanes are mainly devoted to increasing the bandwidth. Backplane bandwidth is defined as the product of the data-bus width and the data rate for each bus channel. Increasing the number of the bus lines can thus multiply the bus bandwidth. However, as the bandwidth requirement of board-level and chip-level interconnects is projected to reach tens of terabits per second (Tb/s), even waveguide-based interconnections cannot meet the potential bandwidth challenge. Additionally, waveguide-based optical interconnects still have physical limitations when compared to free-space optical links.

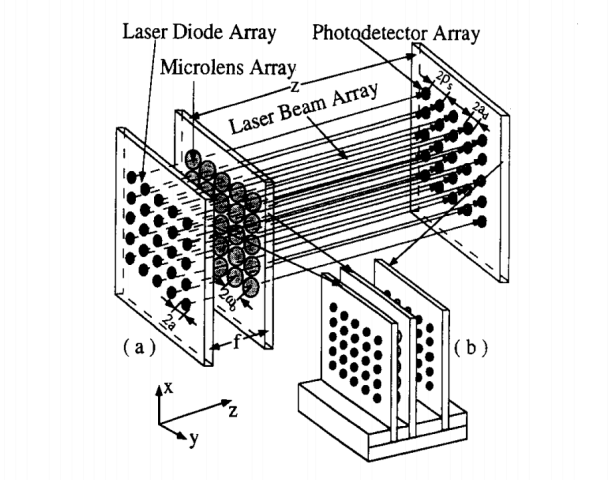

Figure 1.3: A schematic illustration of point-to-point free-space interconnects, reprinted with permission from [26].

By contrast, free-space optical interconnect is a technology for transmitting information without waveguides or fibers, in which a beam propagates between the computer's components through free space. Figure 1.3 shows a schematic illustration of free-space interconnects, which could be applied as a board-to-board parallel optical link with direct termination of optical signals on-chip [26]. There are applications where multiple parallel channels are required and the interconnect configuration is more complex than a simple point-to-point link in high-end system including multiprocessor computers, telecommunications switches, and servers. Therefore, 3D free-space optical backplane architectures have also been proposed to link multiple boards and chips.

Continued device scaling enables microprocessors and other systems-on-chip (SoCs) to increase their performance. In the free-space optical interconnect system, 3-D integration technologies enable electro-optical system-in package (SiP), which are utilized to electrically connect the free space and photonics layers with the electronics [27]. The GaAs chip is flip-chip bonded to the backside of the silicon chip, and connected to the transceiver circuits using through-silicon-vias. It can be clearly seen that natural 3-D arrangement capabilities of free-space optical links with out-of-plane links can potentially provide a high-density optical bandwidth [28]. Such free-space optical links have less crosstalk and less wiring congestion issues compared with waveguides. Moreover, it requires less

manufacturing and packaging process for free-space interconnects, as fewer physical contacts are needed between the laser source and the receiver.

1.2. Optical Modulators for Optical Communication Networks

External modulation offers several advantages compared to direct modulation: the optical source can be relatively inexpensive and its operation does not need to be compromised by direct modulation. Modulation speed can be higher, and direct phase modulation can be realized by external modulation mechanism [29-31]. Furthermore, light from a single light source can be routed into multiple channels controlled by individual modulators. This could further reduce the total power budget of the entire system.

Although existing photonic technologies using directly modulated VCSELs have readily enabled parallel or 3-D optical interconnects, wavelength chirp has discouraged direct modulation for VCSELs and limits the modulation bandwidth. Optical injection locking has been investigated and could reduce the VCSEL chirp and nonlinear distortions, but such technology significantly adds complexity to the system [32-33]. Therefore, external modulators with ultra-compact footprint, high efficiency, low loss and power consumption are requirement in the development of high-speed optical communications networks.

1.2.1. Overview of Modulation Mechanism

The necessity of a modulator in an optical link has been discussed previously. An optical modulator can alter different beam parameters, such as

amplitude, phase, or polarization. In addition, light modulation mechanism can be also classified into thermo-optical effect, electro-optic (E-O) effect, and electroabsorption effect.

Thermo-optic effect is based on thermal modulation of the refractive index of a material. For example, the refractive index of silicon can be tuned via resistive heating [34]. Although thermal modulation is too slow for the high frequencies required in modern communication applications, thermal modulation is still useful to demonstrate operational devices during first-stage research.

Electro-optic and electroabsorption effects are predominately utilized for ultrafast compact optical modulators [29-31, 35-38]. Electro-optic effect originates from the application of an electric field to a material, which can result in changes to refractive indices. The electro-optic effect includes Pockels effect, Kerr effect, and carrier effect in general. Those most common electro-optic effects found in compound semiconductors are inherently weak in silicon. The most common modulation method used in silicon devices is the plasma dispersion effect [39]. This effect is based on the modulation of real and imaginary part of the refractive index due to the change of concentration of free charges in silicon.

Electroabsorption devices involve the quantum-confined Stark effect (QCSE) or the Franz–Keldysh effect (FKE) [40-41]. The QCSE devices are based on electric-field induced changes in optical absorption in quantum-well structures, which consist of heterojunctions formed by a small bandgap material sandwiched between two layers of a larger-bandgap material [40]. QCSE has more spectrally

abrupt and stronger changes in absorption coefficient compared to FKE, which occurs in bulk semiconductors.

By combining the aforementioned individual effect (i.e. Pockels, Kerr, and QCSE) with design features of devices, a high-performance optical modulator could be realized. Those designs including cavity resonators, hybrid waveguides, surface plasmon resonance in periodic structures, photonic crystals and slot waveguide, have been intensively investigated to enhance those effects in light-matter interactions [29-31, 42-44].

Overall, the three major considerations for utilizing an optical modulator are power consumption, available bandwidth, and packing density. We believe that the leading candidate technology for an ultra-compact modulator is plasmonics, which is based on the surface plasmon polaritons (SPPs) excitation at the metal and dielectric interface [45]. Such technology enables nanoscale light-matter interactions, which overcomes the diffraction limit in conventional optical devices. Seagate has adopted plasmonics in near-field transducer design for heat-assisted magnetic recording to increase storage density [46].

Summary of the ultrafast wavelength-size electro-optic modulators can be found in reference [47], which indicates that the performance for the modulators depends on the capability to increase the inherently weak interaction between matter and photons. By combining the aforementioned individual effects with SPP effect, hybrid devices will enable ultra-high-speed modulation with efficient bit energy consumption. Fundamental analysis has shown that electro-optic

modulators could enable bit energy consumption of ~1 fJ/bit efficiency with over 100 Gbps data rate for a single channel. However, challenges are still faced by researchers including high loss, process compatibility and integration for drivers in the devices.

1.2.2. Free-Space Modulators based on Surface-Normal Modulation

Taking advantage of VCSEL arrays, free-space optical modulators can potentially meet the bandwidth requirement for future 3-D parallel optical interconnects [17-19]. Surface-normal modulators could enable direct modulation of the light beams from VCSEL arrays without introducing other components, like micromirrors. In addition, surface-normal modulators also have smaller size with better packaging compatibility. Figure 1.4 shows the schematic illustration of a surface normal modulator that could potentially be applied to board-to-board interconnects. Such system has an application for future short-distance optical interconnects, which potentially plays a significant role in telecommunication, free-space optical communication and RF photonic systems as they have higher coupling efficiency with single mode fibers compared with waveguide modulators.

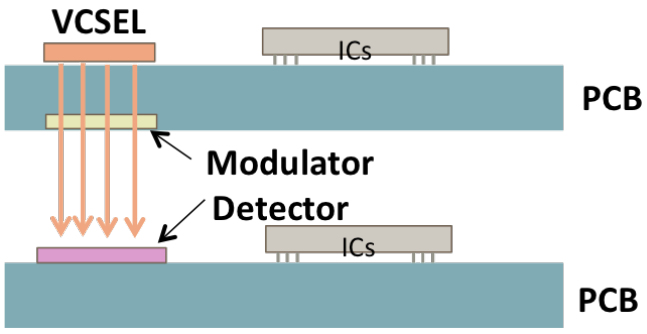

Figure 1.4: The schematic illustration of a surface normal modulator board-to-board interconnects.

There are two existing device structures for surface-normal optical modulators based on Quantum-Confined Stark effect (QCSE) and cavity effect [40, 48-50]. The QCSE-based surface-normal modulator is shown in Figure 1.5 [40], which changes the light absorption when subjected to an external voltage. Such modulator could achieve a high extinction ratio and reduce chirp effect compared with direct modulation of a laser diode. The device consists of an ultra-thin quantum-well layer based on the epitaxial growth of III-V semiconductors. A large absorption area is required for this device, which will increase the time delay due to the resistance-capacitance (RC) constant. In addition, the epitaxial growth of III-V semiconductors or strained Ge/Si is cost-ineffective, which prevents the mass production of the devices for photonic integration.

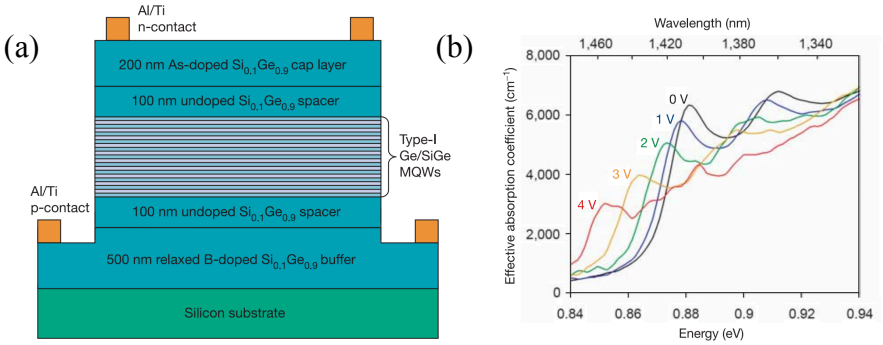

Figure 1.5: (a) The structure of a modulator based on quantum-confined Stark effect (QCSE); (b) modulation of absorption with controlled voltage, reprinted with permission from [40].

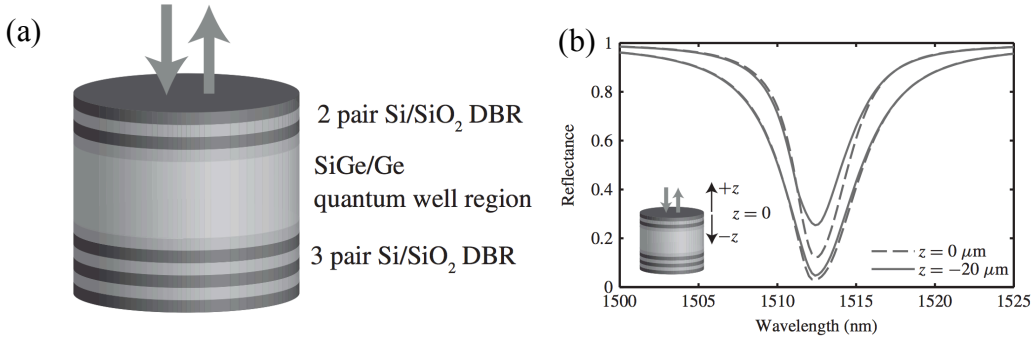

Figure 1.6: (a) The structure of a modulator based on Fabry-Perot effect; (b) intensity modulation of reflectance of the device, reprinted with permission from [49].

The other surface-normal modulator structure uses high-Q Fabry-Perot (F-P) resonant cavities, as shown in Figure 1.6 [49]. However, there is intrinsic trade-

offs between energy efficiency and modulation bandwidth for an F-P resonator. The Lorentzian formula that was regarded as the fundamental lineshape of resonance cannot simultaneously achieve a sharp transitional edge for high energy efficiency and a broad bandpass for high-speed data transmission, because amplitude modulation inherently requires a modulation bandwidth that doubles the modulation frequency. From the physics perspective, we can understand this compromise arising from the photon lifetime of high-Q resonators, which takes a relatively long time to build up the resonant mode and to decay the optical field inside a high-Q cavity. As a result, high-Q resonant photonic devices have invincible drawbacks in ultrahigh frequency E-O modulation, although they have undisputable potentials in optical sensors and optical interconnects with moderate modulation speed (~10Gbps). This intrinsic drawback has been experimentally confirmed using E-O polymer ring resonators, which shows non-uniform oscillating normalized response for every 20 GHz frequency.

In conclusion, surface-normal optical modulators need to be low-cost, energy efficient and have large available bandwidth with expandability to modulator arrays. Current technologies cannot meet those requirements based on aforementioned discussion. We believe that plasmonics is the leading candidate technology for next generation free-space optical interconnect systems, which will provide ultra-compact solutions for surface-normal modulation.

1.3. Plasmonic Modulation for Ultra-Compact Solutions

1.3.1. Surface Plasmon Resonances

Although silicon modulators have been demonstrated with merits of large RF bandwidth using a travelling wave modulator, compactness using a photonic-crystal modulator and the energy efficiency using a ring modulator [29, 34, 51]. The plasmonic modulator has been investigated during the past, which could combine all the merits mentioned above and show supreme advantages compared with silicon-based devices [44, 52-53].

Surface plasmon resonances arise from the excitation of surface collective oscillations of electrons [54]. There has been a significant advance in both theoretical and experimental investigations of surface plasmon resonances, which have been employed in a wide spectrum of studies in electrochemistry, biosensing, surface plasmon microscopy, modulation and optical switching. Plasmonics offers a unique opportunity to bring down the size of optical components. The large permittivity contrast at the metal/dielectric interface allows the SPPs to be confined to the subwavelength areas. Thus, plasmonics can be considered as an alternative path towards a new generation of more densely integrated photonic circuits with dimensions that would not be possible by any other conventional photonic technology.

Figure 1.7(a) and Figure 1.7(b) illustrate the difference between propagating and localized surface plasmons. In the case of surface plasmon polaritons,

plasmons propagate in the x- and y-directions along the metal-dielectric interface, and decay evanescently in the z-direction. The propagation length of the surface plasmon polaritons in Figure 1.7(a) is on the order of tens to hundreds of micron [55]. Localized surface plasmons (LSPs) are charge density oscillations at the surfaces of metallic nanoparticles and metallic nanostructures (Figure 1.7(b)) [56]. Excitation of LSPs by incident light with resonant wavelength results in strong light scattering, intense surface plasmon (SP) absorption bands, and an enhancement of the local electromagnetic fields [57]. Intensive studies in surface plasmons have come from recent advances in the investigation of the electromagnetic properties of nanostructured materials. The wavelength and intensity of the SP absorption are characteristic of the type of metals, and are highly sensitive to the size, shape of the nanostructures, and the surrounding dielectric medium. These are the properties and mechanisms that have prompted the ongoing studies in LSP-based sensors and devices.

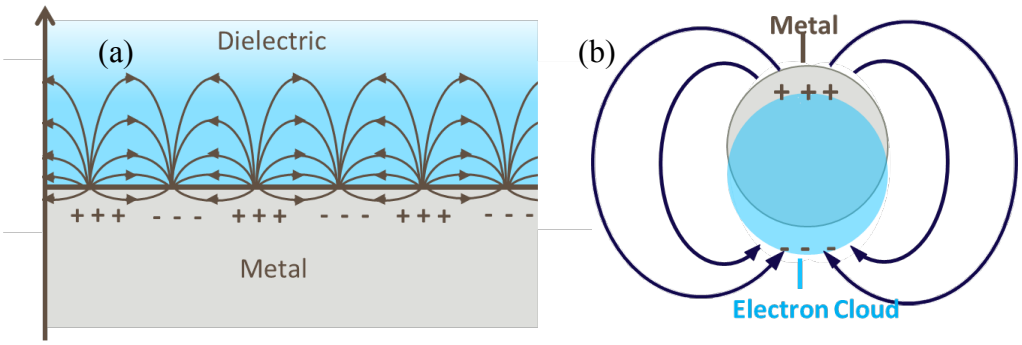

Figure 1.7: (a) Surface plasmon polaritons at metal and dielectric interface; (b) localized surface plasmon resonance at the metal surface [49].

1.3.2. Fano Resonances in Metallic Photonic Crystals

One of the most attractive aspects of the surface plasmon resonances now is their use to concentrate light in subwavelength structures and to enhance transmission through periodic arrays of subwavelength holes or narrow slits in metal films [58-62]. Extraordinary optical transmission (EOT) through subwavelength structures has been the subject of intensive research in plasmonics for many years. The mechanisms underlying the EOT in these grating or photonic crystal systems can be attributed to the complex interaction among SPPs, Rayleigh Anomalies (RAs), waveguide modes, and even the Fabry-Perot (FP) resonances inside the airholes or slits. For the simplest structure consisting of a thin metallic grating on top of a glass substrate as shown in Figure 1.8(a), waveguide modes and F-P resonances inside the slits are not supported, therefore, the EOT phenomenon is described by the coupling of RAs on one side the film with SPP Bloch waves (SPP-BWs) on the opposite side. RAs originated from the observations by Wood as early as 1902 and were physically interpreted by Rayleigh and Fano as the passing-off of a spectral diffraction order, and are associated with both plasmonic and dielectric gratings.

The structure consists of a one-dimensional (1-D) periodic gold (Au) array structure on a glass substrate with refractive index n of 1.502 as shown in Figure 1.8(a). The Au film thickness is 100 nm, the grating period is 1140 nm and the gap width is 100 nm, as shown in the cross-sectional view in Figure 1.8(b). When a transverse-magnetic(TM) plane wave excites the plasmonic grating from the top

with an incident angle of θ, the grating with periodicity p will add additional photon momentum in integer multiples of G = 2π/p in the x direction. In this case, SPPs are excited under the phase matching condition [63],

$$k_{SPP} = k_0 \sin\theta \pm iG = \mathrm{Re}\left|\frac{\omega}{c}\sqrt{\frac{\varepsilon_{Au}\varepsilon_d}{\varepsilon_{Au}+\varepsilon_d}}\right| \tag{1.1}$$

where ω, c, and k_0 are the angular frequency, velocity, and momentum of light in free space, ε_d and ε_{Au} are the dielectric permittivity of the dielectric medium and Au, respectively. i is an integer which denotes specific SPP mode, and θ is the incident angle. Besides SPP waves, RAs are excited as well, which come from the diffracted wave propagating parallel to the grating surface. RAs occur under the condition [64],

$$k_{RA} = k_0 \sin\theta \pm iG = \mathrm{Re}\left|\frac{\omega}{c}\sqrt{\varepsilon_d}\right| \tag{1.2}$$

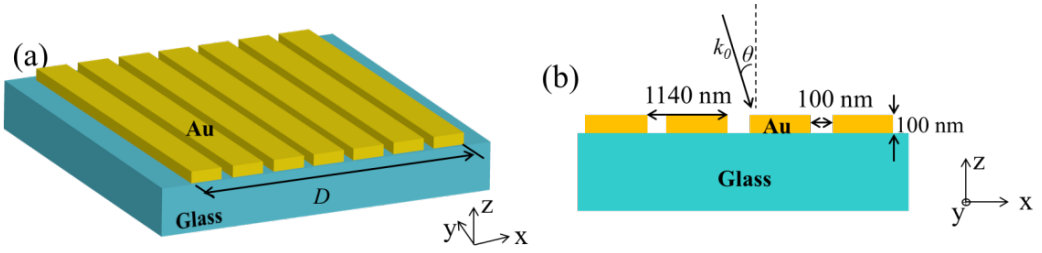

Figure 1.8: (a) The schematic illustration of the finite Au grating on a glass substrate; (b) cross-sectional view of the structure with geometric parameters.

Figure 1.9 shows a modulation scheme where the intensity of an optical spectrum is modulated by an external RF signal. The applying voltage induces a spectrum shift, which results in intensity change at λ_0 measured by a photodetector. By using a single-wavelength laser with output at λ_0, the "on" and

"off" optical states are observed and could be converted by to electrical signal using a photodetector. Extinction ratio is the ratio of two optical power levels, as shown in Figure 1.9.

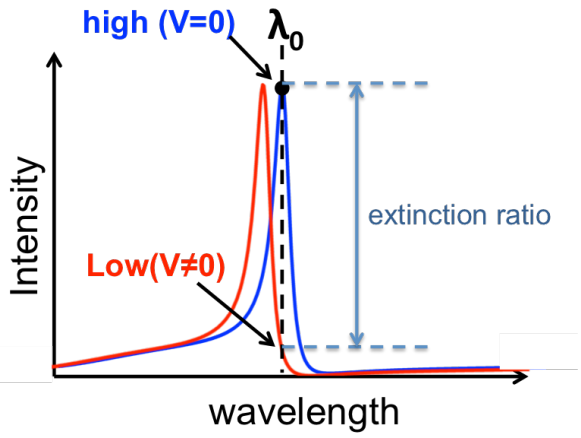

Figure 1.9: Schematic illustration of intensity modulation.

Figure 1.10 shows the surface-normal modulation of harmonic generation of light from a plasmonic nanocavity filled with a nonlinear medium, taken from [65]. The plasmonic device shows electric field induced second harmonic generation consisting of a gold nanoslit resonator surrounded by a grating-based optical nanostructure. The two electrodes were wire-bonded to external circuits in order to apply an external voltage. A fundamental wave at 1.56 μm was frequency doubled and modulated in intensity by the external voltage. Such surface-normal plasmonic modulators offer a new route to develop ultracompact optical devices on a chip by using extreme light concentration to nanoscale and the ability to

perform simultaneous electrical and optical functions at ultra-high speed operation.

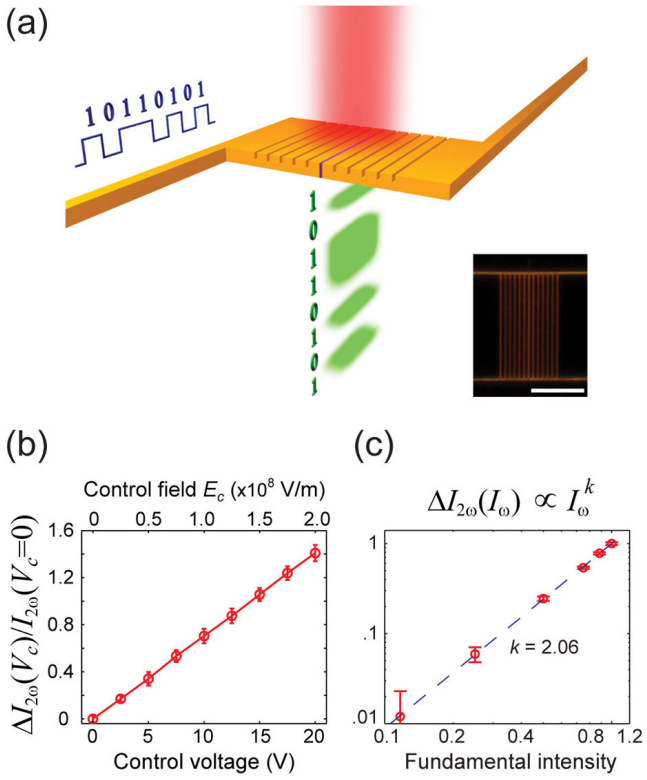

Figure 1.10: An example of surface-normal modulation in a plasmonic nanostructure, reprinted with permission from [65]. (a) the schematic illustration of device structure for modulation; (b) the induced nonlinear output as a function of external voltage; (c) the nonlinear output as a function of the fundamental wave.

1.4. Thesis Organization

Chapter 2 will show the actively control of the optical transmission in a metallic photonic crystal with moderate refractive index modulation by thermo-optic effect. The design of the Fano resonance with a sharp transitional edge in

the metallic photonic crystal is discussed in detail. Index modulation due to thermo-optic effect is presented in this chapter.

Chapter 3 presents the electro-optic modulation using hybrid polymer and plasmonic structures. Fabrication of these structures and the experimental measurement results are presented in this chapter. Electro-optic modulation of the hybrid plasmonic-organic structures will lead to an ultra-compact device with fast modulation and low driving voltage.

The focus of Chapter 4 will be the development of all-optical switching processing devices based on the hybrid plasmonic-organic structure. The effectiveness of enhancing the nonlinearity through plasmonic effect is demonstrated.

The effect of finite metallic grating size on the resonances will be presented in Chapter 5. A simple method is presented based on the combination of RCWA and finite aperture diffraction. This study effectively demonstrates the theoretical limit of miniaturizing subwavelength plasmonic gratings for sensing and optical modulation applications without using 3D full wave simulator.

A brief summary and conclusion will be presented in Chapter 6.

Reference

[1] R. Ho, K. W. Mai and M. A. Horowitz, “The future of wires,” Proc. IEEE, 89, 490-504(2001).

[2] D. A. B. Miller, "Physical reasons for optical interconnection," Int. J. Optoelectron., 11, 155-168(1997).

[3] D. A. B. Miller and H. M. Ozaktas, “Limit to the bit-rate capacity of electrical interconnects from the aspect ratio of the system architecture,” J. Parallel Distrib. Comput., 41, 42-52(1997).

[4] F. Benner, M. Ignatowski, J. A. Kash, D. M. Kuchta and M. B. Ritter, “Exploitation of optical interconnects in future server architectures,” IBM J. Res. Develop., 49, 755-775(2005).

[5] E. Mohammed, A. Alduino, T. Thomas, H. Braunisch, D. Lu, J. Heck, A. Liu, I. Young, B. Barnett, G. Vandentop and R. Mooney, “Optical interconnect system integration for ultra-short-reach applications,” J. Intel. Technol., 8, 115-127(2004).

[6] Shacham, K. Bergman and L. P. Carloni, “Photonic networks-on-chip for future generations of chip multiprocessors,” IEEE Trans. Comput., 57, 1246-1260(2008).

[7] D. A. B. Miller, “Optical interconnects to silicon,” IEEE J. Sel. Topics Quantum Electron., 6, 1312-1317(2000).

[8] X. Z. Zheng, P. J. Marchand, D. W. Huang and S. C. Esener, "Free-space parallel multichip interconnection system," Appl. Optics, 39, 3516-3524(2000).

[9] J. S. Levy, A. Gondarenko, M. A. Foster, A. C. Turner-Foster, A. L. Gaeta and M. Lipson, "CMOS-compatible multiple-wavelength oscillator for on-chip optical interconnects." Nature Photon., 4, 37-40(2010).

[10]M. Haurylau, G. Chen, H. Chen, J. Zhang, N. A. Nelson, D. H. Albonesi, E. G. Friedman and P. M. Fauchet, "On-chip optical interconnect roadmap: challenges and critical directions," IEEE J. Sel. Topics Quantum Electron., 12, 1699(2006).

[11]G. Kirk, D. V. Plant, T. H. Szymanski, Z. G. Vranesic, F. A. P. Tooley, D. R. Rolston, M. H.Ayliffe, F. K. Lacroix, B. Robertson, E. Bernier and D. F. Brosseau, “Design and implementation of a modulator-based freespace optical backplane for multiprocessor applications,” Appl. Opt., 42, 2465-2481(2003).

[12]D. V. Plant, M. B. Venditti, E. Laprise, J. Faucher, K. Razavi, M. Chateauneuf, A. G. Kirk and J. D. Ahearn, “A 256 channel bi-directional optical interconnect using VCSELs and photodiodes on CMOS,” IEEE J. Lightwave Technol., 19, 1093-1103(2001).

[13]H. S. Harvard, "Progress in systems based on free-space interconnection," In OE/LASE'93: Optics, Electro-Optics, & Laser Applications in Science& Engineering, International Society for Optics and Photonics, 2-3(1993).

[14]C. J. Henderson, D. G. Leyva and T. D. Wilkinson, “Free space adaptive optical interconnect at 1.25 Gb/s, with beam steering using a ferroelectric liquid-crystal SLM,” J. Lightw. Technol., 24, 5, 1989(2006).

[15]K. Wang, A. Nirmalathas, C. Lim, E. Skafidas and K. Alameh, "Experimental demonstration of 3×3 10 Gb/s reconfigurable free space optical card-to-card interconnects", Opt. Lett., 37, 2553-2555 (2011).

[16]K. Wang, A. Nirmalathas, C. Lim, E. Skafidas and K. Alameh, "Experimental demonstration of high-speed freespace reconfigurable card-to-card optical interconnects," Opt. Express, 21, 2850 (2013).

[17]Y. C. Chang, C. S. Wang and L. A. Coldren, "High-efficiency, high-speed VCSELs with 35 Gbit/s error-free operation," Electron. Lett., 43, 1022-1023(2007).

[18]P. Westbergh, J. S. Gustavsson, B. Kögel, A. Haglund, A. Larsson, A. Mutig, A. Nadtochiy, D. Bimberg and A. Joel, “40 Gbit/s error-free operation of oxide-confined 850 nm VCSEL,” Electron. Lett., 46, 1(2010).

[19]P. Westbergh, R. Safaisini, E. Haglund, B. Kögel, J. S. Gustavsson, A. Larsson, M. Geen, R. Lawrence and A. Joel, “High-speed 850 nm VCSELs with 28 GHz modulation bandwidth operating error-free up to 44 Gbit/s,” Electron. Lett., 48, 1(2012).

[20]Semiconductor Industry Association, International Technology Roadmap for Semiconductors: 1999 Edition. Austin, TX: International SEMATECH, 1999.

[21]A. G. Kirk, D. V. Plant, M. H. Ayliffe, M. Châteauneuf and F. Lacroix, “Design rules for highly parallel free-space optical interconnects,” IEEE J. Sel. Topics Quantum Electron., 9, 531-547(2003).

[22]M. Châteauneuf, A. G. Kirk, D. V. Plant, T. Yamamoto, J. D. Ahearn and W. Luo, “512-channel vertical-cavity surface-emitting laser based free-space optical link,” Appl. Opt., 41, 5552-5561(2002).

[23]X. Dou, A. X. Wang, X. Lin and R. T. Chen, "Photolithography-free polymer optical waveguide arrays for optical backplane bus," Opt. Express, 19, 14403-14410 (2011).

[24]K. B. Yoon, I. K. Cho, S. H. Ahn, M. Y. Jeong, D. J. Lee, Y. U. Heo, B. S. Rho, H. H. Park and B. H. Rhee, “Optical backplane system using waveguide-embedded PCBs and optical slots,” J. Lightwave Technol., 22, 2119-2127(2004).

[25]K. Schmidtke, F. Flens, A. Worrall, R. Pitwon, F. Betschon, T. Lamprecht and R. Krähenbühl, “960 Gb/s optical backplane ecosystem using embedded polymer waveguides and demonstration in a 12G SAS storage array,” J. Lightwave Technol., 31, 3970-3975(2013).

[26]S. Tang, R. T. Chen, L. Garrett, D. J. Gerold and M. M. Li, “Design limitations of highly parallel free-space optical interconnects based on arrays of vertical-cavity surface-emitting laser diodes, microlenses, and photodetectors,” J. Lightwave Technol., 12, 1971-1975 (1994).

[27]J. Xue, A. Garg, B. Ciftcioglu, J. Hu, S. Wang, I. Savidis, M. Jain, R. Berman, P. Liu, M. Huang and H. Wu, “An intra-chip free-space optical interconnect,” In ACM SIGARCH Computer Architecture News, 38, 94-105(2010).

[28]B. Ciftcioglu, R. Berman, S. Wang, J. Hu, I. Savidis, M. Jain, D. Moore, M. Huang, E. G. Friedman, G. Wicks and H. Wu, "3-D integrated heterogeneous intra-chip free-space optical interconnect," Opt. Express, 20, 4331-4345 (2012).

[29]A. Liu, R. Jones, L. Liao, D. Samara-Rubio, D. Rubin, O. Cohen, R. Nicolaescu and M. Paniccia, "A high-speed silicon optical modulator based on a metal-oxide-semiconductor capacitor," Nature, 427, 615-618 (2004).

[30]M. Liu, X. Yin, E. Ulin-Avila, B. Geng, T. Zentgraf, L. Ju, F. Wang and X. Zhang, “A graphene-based broadband optical modulator,” Nature, 474, 64-67(2011).

[31]Q. Xu, B. Schmidt, S. Pradhan and M. Lipson, “Micrometre-scale silicon electro-optic modulator,” Nature, 435, 325-327(2005).

[32]C. H. Chang, L. Chrostowski and C. J. Chang-Hasnain, “Injection locking of VCSELs,” IEEE J. Sel. Topics Quantum Electron., 9, 1386-1393(2003).

[33]L. Chrostowski, C.H. Chang and C. J. Chang-Hasnain, “Enhancement of dynamic range in 1.55-μm VCSELs using injection locking,” IEEE Photon. Technol. Lett., 15, 498-500(2003).

[34]L. Gu, W. Jiang, X. Chen and R.T. Chen, "Thermooptically tuned photonic crystal waveguide silicon-on-insulator Mach-Zehnder interferometers," IEEE Photon. Technol. Lett., 19, 342(2007).

[35]B. Chmielak, M. Waldow, C. Matheisen, C. Ripperda, J. Bolten, T. Wahlbrink, M. Nagel, F. Merget and H. Kurz, "Pockels effect based fully integrated, strained silicon electro-optic modulator," Opt. Express, 19, 17212-17219(2011).

[36]J. F. Vinchant, J. A. Cavailles, M. Erman, P. Jarry and M. Renaud, "InP/GaInAsP guided-wave phase modulators based on carrier-induced effects: theory and experiment." J. Lightwave Technol., 10, 63-70(1992).

[37]K. Sato, "Measurement of magneto-optical Kerr effect using piezo-birefringent modulator," Jpn. J. Appl. Phys., 20, 2403(1981).

[38]B. Mason, A. Ougazzaden, C.W. Lentz, K.G. Glogovsky, C. L. Reynolds, G. J. Przybylek, R. E. Leibenguth, T. L. Kercher, J. W. Boardman, M.T. Rader and J. M. Geary, "40-Gb/s tandem electroabsorption modulator," IEEE Photon. Technol. Lett., 14, 27-29 (2002).

[39]G. V. Treyz, P. G. May and J. M. Halbout, "Silicon Mach-Zehnder waveguide interferometers based on the plasma dispersion effect," Appl. Phys. Lett., 59, 771-773(1991).

[40]Y. H. Kuo, Y. K. Lee, Y. Ge, S. Ren, J. E. Roth, T. I. Kamins, D. A. Miller and J. S. Harris, "Strong quantum-confined Stark effect in

germanium quantum-well structures on silicon," Nature, 437, 1334-1336(2005).

[41]Y. Yacoby, "High-frequency Franz-Keldysh effect," Phys. Rev., 169(3), 610(1968).

[42]F. Ren, M. Li, Q. Gao, W. Cowell, J. Luo, A. K. Jen and A. X. Wang, "Surface-normal plasmonic modulator using sub-wavelength metal grating on electro-optic polymer thin film," Opt. Commun., 352, 116-120(2015).

[43]C. Husko, A. De Rossi, S. Combrié, Q. V. Tran, F. Raineri and C. W. Wong, "Ultrafast all-optical modulation in GaAs photonic crystal cavities," Appl. Phys. Lett., 94, 021111(2009).

[44]W. Cai, J. S. White and M. L. Brongersma, "Compact, high-speed and power-efficient electrooptic plasmonic modulators," Nano Lett., 9, 4403-4411(2009).

[45]E. Ozbay, "Plasmonics: merging photonics and electronics at nanoscale dimensions," Science, 311, 189-193 (2006).

[46]N. Zhou, Xu, X., A. T. Hammack, B. C. Stipe, K. Gao, W. Scholz and E.C. Gage, "Plasmonic near-field transducer for heat-assisted magnetic recording," Nanophotonics, 3, 141-155(2014).

[47]K. Liu, C. R. Ye, S. Khan and V. J. Sorger, "Review and perspective on ultrafast wavelength size electro-optic modulators," Laser Photon. Rev., 9, 172-194(2015).

[48]H. Mohseni, W. K. Chan, H. An, A. Ulmer and D. Capewell, "Tunable surface-normal modulators operating near 1550 nm with a high-extinction ratio at high temperatures," IEEE Photon. Technol. Lett., 18, 214-216 (2006).

[49]R. M. Audet, E. H. Edwards, P. Wahl and D. A. Miller, "Investigation of limits to the optical performance of asymmetric Fabry-Perot electroabsorption modulators," IEEE J. Quan. Electron., 48, 198-209 (2012).

[50]Q. Wang, S. Junique, D. Agren, B. Noharet and J. Y. Andersson, "Fabry-Perot electroabsorption modulators for high-speed free-space optical communication," IEEE Photon. Technol. Lett., 16, 1471-1473 (2004).

[51]X. Wang, C-Y Lin, S. Chakravarty and R. T. Chen, "Effective in-device r_{33} of 735pm/V on electro-optic polymer infiltrated silicon photonic crystal slot waveguide," Opt. Letters, 36, 882-884 (2011).

[52]A. Melikyan, L. Alloatti, A. Muslija, D. Hillerkuss, P. C. Schindler, J. Li, R. Palmer, D. Korn, S. Muehlbrandt, D. Van Thourhout, B. Chen, R. Dinu, M. Sommer, C. Koos, M. Kohl, W. Freude and J. Leuthold, "High-speed plasmonic phase modulators," Nature Photon., 8, 229-233(2014).

[53]C. Haffner, W. Heni, Y. Fedoryshyn, J. Niegemann, A. Melikyan, D. L. Elder, B. Baeuerle, Y. Salamin, A. Josten, U. Koch and C. Hoessbacher, "All-plasmonic Mach-Zehnder modulator enabling optical high-speed communication at the microscale," Nature Photon., 9, 525-528(2015).

[54]W. Knoll, "Interfaces and thin films as seen by bound electromagnetic waves," Annu. Rev. Phys. Chem., 49, 569-638(2001).

[55]E. Hutter and J. H. Fendler, “Exploitation of localized surface plasmon resonance,” Adv. Mater., 16, 1685-706(2004).

[56]K. A. Willets and R. P. Van Duyne, “Localized surface plasmon resonance spectroscopy and sensing," Annu. Rev. Phys. Chem., 5, 267-297(2007).

[57]J. Haes and R. P. Van Duyne, “A nanoscale optical biosensor: sensitivity and selectivity of an approach based on the localized surface plasmon resonance spectroscopy of triangular silver nanoparticles,” J. Am. Chem. Soc., 124, 10596-10604(2002).

[58]J. A. Porto, F. J. García-Vidal and J. B. Pendry, "Transmission resonances on metallic gratings with very narrow slits," Phys. Rev. Lett., 83, 2845-2848 (1999).

[59]H. J. Lezec, A. Degiron, E. Devaux, R. A. Linke, L. Martin-Moreno, F. J. Garcia-Vidal and T. W. Ebbesen. “Beaming light from a subwavelength aperture,” Science, 297, 820-822(2002).

[60]A. Christ, S. G. Tikhodeev, N. A. Gippius, J. Kuhl and H. Giessen, "Waveguide-plasmon polaritons: Strong coupling of photonic and electronic resonances in a metallic photonic crystal slab," Phys. Rev. Lett., 91, 183901 (2003).

[61]R. W. Wood, “On a remarkable case of uneven distribution of light in a

diffraction grating spectrum," Philos. Mag., 4, 269-275 (1902).

[62]L. Rayleigh, "Note on the remarkable case of diffraction spectra described by Prof. Wood," Philos. Mag., 14, 60–65 (1907).

[63]H. R. Raether, Surface plasmons on smooth surfaces and Rough Surfaces (Springer, 1988).

[64]R. W. Wood, "Anomalous diffraction gratings." Phys. Rev., 48, 928(1935).

[65]W. Cai, A. P. Vasudev and M. L. Brongersma, "Electrically controlled nonlinear generation of light with plasmonics," Science, 333, 1720-1723(2011).

CHAPTER 2. THERMO-OPTIC MODULATION OF FANO RESONANCES IN METALLIC PHOTONIC CRYSTALS

In this chapter, we present theoretical design and experimental demonstration of a metallic photonic crystal slab using a simple gold (Au) grating with subwavelength slits on glass substrates. Periodic metallic structures with subwavelength features, which are usually referred as metallic photonic crystals, provide simultaneous electronic and photonic resonances in the same energy range, leading to highly unique properties such as extraordinary optical transmission (EOT), photonic bandgap, Fano resonances, and nonlinear optical effects [1-8]. This unique design provides the possibility to actively control the optical transmission with moderate refractive index modulation that is achievable by thermo-optic effects.

2.1. Theoretical Study

Compared with conventional plasmonic waveguides formed by uniform metal-dielectric thin films or stripes, metallic photonic crystals provide stronger optical mode confinement, smaller device size, and better manipulation to photons [9-18]. Although the optical transmission of metallic photonic crystal slab has been extensively investigated in theory and experimentally characterized [19-23], such plasmonic devices majorly find applications as optical sensors utilizing the resonant frequency shift and localized electric field to enhance the light-matter

interaction. Active control of plasmonic resonances on metallic photonic crystal slabs, which is indispensable for optical communication, is only achieved on exotic material systems such as metal-VO_2 and photo-addressable polymers, which can offer a huge refractive index change ($\Delta n>0.5$) [24-25]. Modulating plasmonic resonances with moderate index perturbation, although has been implemented by long-range surface plasmon polariton (SPP) waveguides, remains to be a challenge on metallic photonic crystal slabs [26-27]. Although such attempt has been reported very recently, demonstration of a real working device is not successful. Our design is based on a metallic photonic crystal slab using a simple gold (Au) grating with subwavelength slits on glass substrates. Unlike conventional SPP resonators with low-Q Lorentzian resonant lineshapes due to the high Ohm-loss at optical frequencies, the discrete guided modes induced by Bragg-grating-modulated SPPs couple to the broadband Fabry-Perot (FP) resonance in the narrow slit, resulting in strong asymmetric Fano resonances with sharp plasmonic bandgaps. This unique design provides the possibility to actively control the optical transmission with moderate refractive index modulation that is achievable by thermo-optic or electro-optic effects.

The optical transmission of the grating in Figure 2.1 is simulated by DiffractMod of RsoftTM, which is based on Rigorous Coupled Wave Analysis (RCWA). At the visible and near infrared wavelength range from 400 nm to 2 μm in Figure 2.2, we can clearly observe the fundamental and 2nd-order grating-modulated SPPs at both the Au-air and Au-glass surfaces, which possess typical

asymmetric lineshape of Fano resonances. We also need to point out the interesting difference of the SPPs between the top and bottom surfaces: the Q-factor of Au-air SPPs is much higher than that of the Au-glass SPPs, indicating a much longer photon lifetime, which is named as “ridge resonance”. However, the sharp transitional edge of the low-Q Au-glass SPPs can still provide the possibility for efficient optical modulation, which is not achievable on a conventional Lorentzian-shape resonance.

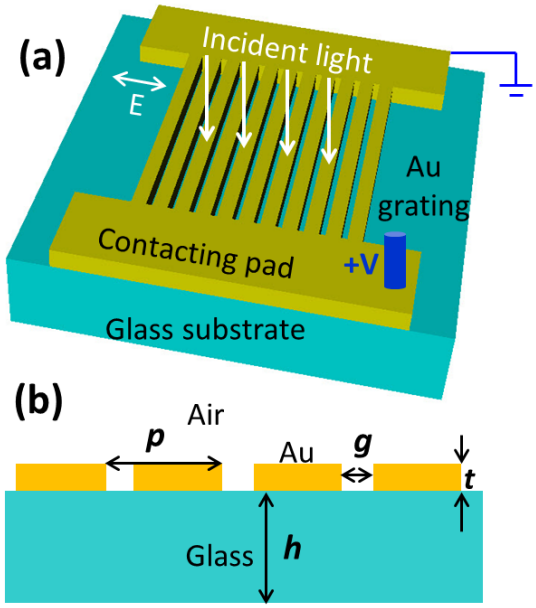

Figure 2.1: (a) Schematic of the proposed metallic photonic crystals; (b) cross-sectional view with geometrical parameters.

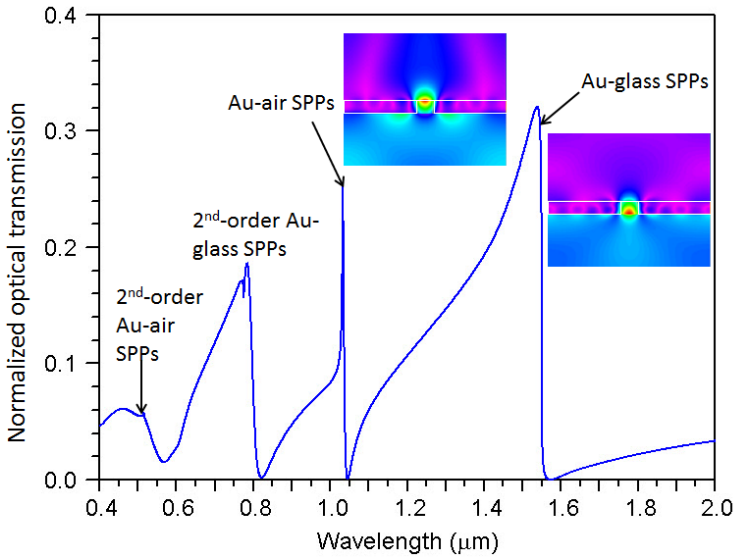

Figure 2.2: Simulated optical transmission of the metallic photonic crystals at visible and near infrared wavelength.

The cross-sectional area of the device is shown in Figure 2.1(b). The device consists of an Au grating region with electric connecting pads. To actively modulate the optical transmission, the applied electric voltage induces current passing through gold wires, which heats the adjacent glass medium. Thermo-optic modulation is achieved by turning on and off of the heating to the glass dielectric medium. When incident light is surface-normally coupled into the metallic grating from a single mode fiber, the transmitted light intensity change is in response to the refractive index perturbation of the glass substrate.

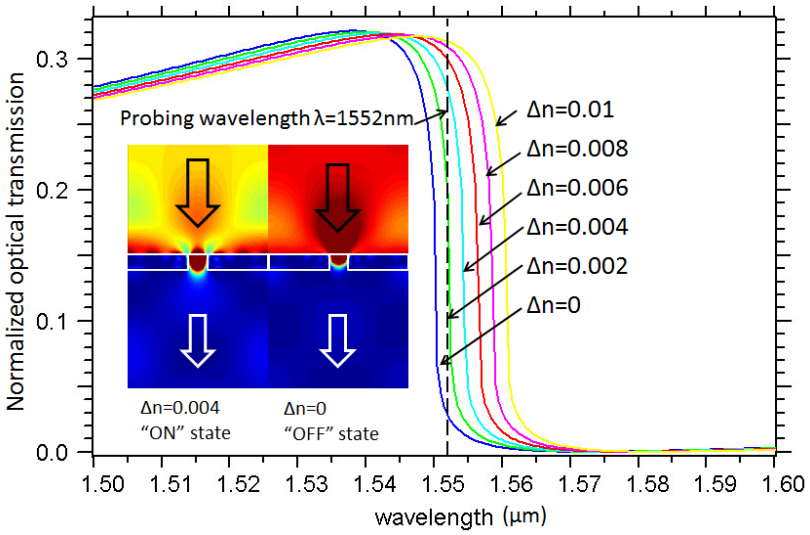

Figure 2.3: Simulated transmission spectrum with different index modulation. The inset figure shows the "ON" and "OFF" state optical intensity distribution of the probing wavelength at 1552nm.

To verify this prediction, we simulate the optical transmission of the metallic photonic crystals with index modulation of the glass substrate from 0 to 0.01. The wavelength range is focused from 1.5 to 1.6 μm. Figure 2.3 proves that increasing the refractive index of the glass substrate red-shifts the transmission spectrum. With a probing wavelength of 1552 nm, the simulated optical intensity distribution suggests that a slight index modulation of 0.004 is sufficient to cut off the resonant mode in the metal slits, giving an optical transmission modulation from 5% to 28%.

2.2. Experimental Characterization

We started the fabrication processes by cleaning a 1"×1" Corning 1737 AMLCD glass substrate with acetone, isopropyl alcohol (IPA), and de-ionized water. A 100 nm gold thin film was deposited by thermal evaporation with the deposition rate at 8 Å/s. The large size electrode pads were patterned by conventional photolithography followed by wet etching in gold etchant. After that, the Au slits are milled using a focused-ion beam (FIB) microscope (Quanta 3D, FEI Company). By directly applying ion-beam lithography, the width the Au slits was controlled to be 100 nm. The design patterns were precisely defined by ion-beam current and dose. For the structure described in this chapter, the beam current is 14.5 pA, and the ion dose is 7 $\mu C/cm^2$. To achieve better accuracies of the patterns, we used the integrated Nanometer Pattern Generation System (NPGS) in the FIB microscope to control the ion-gun, which gives periodicity errors less than 0.5% and slit width variation of only 2%.

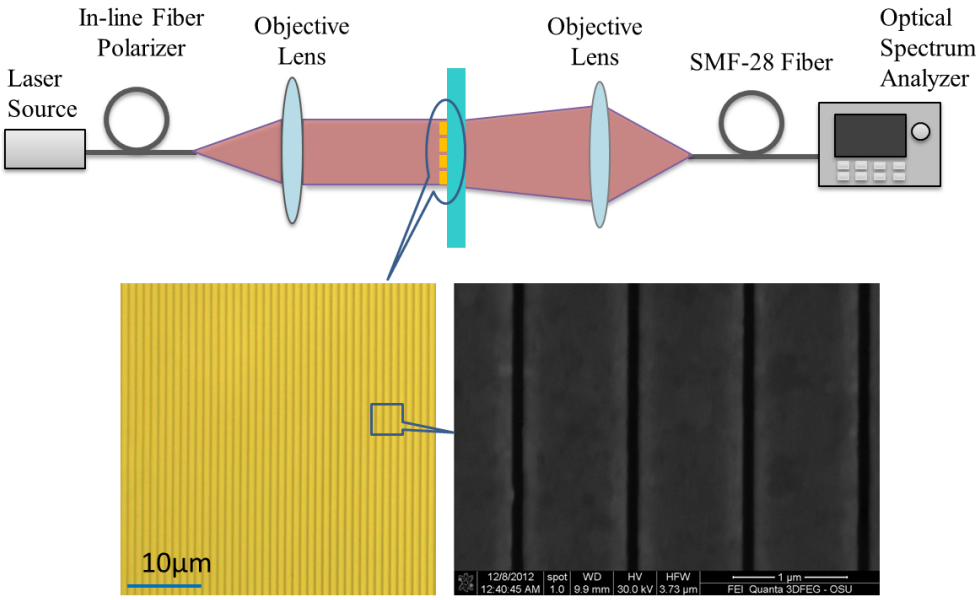

Figure 2.4: Configuration of the experimental setup used for optical transmission setup. The inset optical microscope and SEM picture show the fabricated metallic photonic crystals.

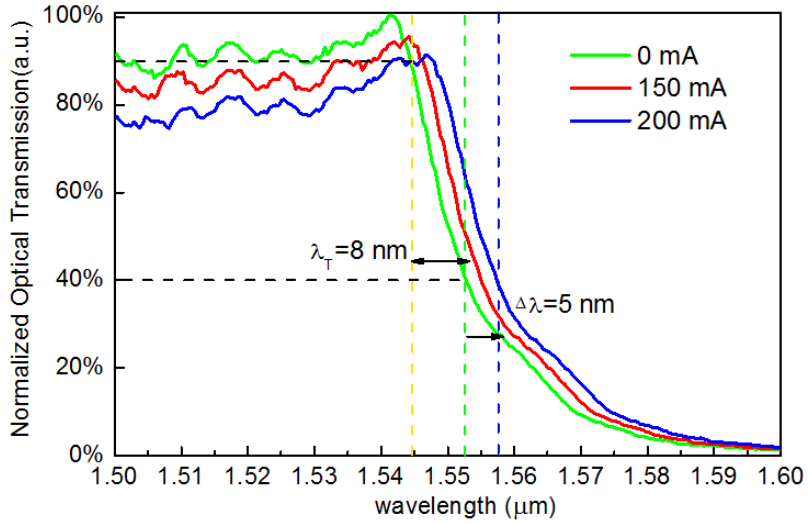

Figure 2.5: Transmission spectra shift due to the index change.

Figure 2.4 shows the experimental setup for measuring the optical transmission. The inset optical microscope and scanning electron microscopy (SEM) picture shows the fabricated metallic photonic crystal slab. A broadband light source from 1.5-1.6μm wavelength was coupled into a single-mode polarization-maintaining (PM) fiber with an in-line fiber polarizer, generating linearly polarized output light that is perpendicular to the grating direction (TM polarization with respect to the grating). The output light was then collimated by a 40× objective lens (NA=0.65). The metallic photonic crystal sample was mounted on a three-dimensional translation/rotation stage, allowing highly precise spatial alignment and angular adjustment with respect to the collimated beam spot. The transmitted beam after the sample was focused by another 40× objective lens, which was then coupled into a standard SMF-28 fiber and measured by an HP 70951A Optical Spectrum Analyzer. To actively control the optical transmission by thermo-optic effects, the Au contacting pads of the metallic photonic crystal slab were wire-bonded and connected with a DC power supply. A multi-meter was used to measure the current flowing through the device. The total serial resistance is measured to be 3.2 Ω by Agilent 4155C semiconductor parameter analyzer with a Karlsuss PA-200 probe station.

Figure 2.5 shows the EOT spectra of the metallic photonic crystal slab recorded at normal incidence. A transitional edge was observed: the relative optical transmission drops from 90% to 40% within only 8nm wavelength. This

measurement qualitatively agrees with the simulated results shown in Figure 2.3, but the transitional edge is not as sharp as what the numerical simulation predicts, which is possibly caused by the fabrication variation and non-perfect beam collimation. A minimum transmission window, or plasmonic photonic bandgap, is observed beyond 1.57μm, which also matches the numerical simulation. Figure 2.4 shows the optical spectra at 0 mA, 150 mA and 200 mA, respectively. Since the refractive index starts to rise when glass substrate is heated by the Au grating, a red shift of the plasmonic resonance occurs, which can be explained by the zero-order relation [28]

$$\lambda_0 = n_{spp} p, \tag{2.1}$$

$$\text{where} \quad n_{spp} = \mathrm{Re}\left(\sqrt{\frac{\varepsilon_{Au}\varepsilon_d}{\varepsilon_{Au}+\varepsilon_d}}\right) \tag{2.2}$$

At 0 mA, n_{spp}=1.518 is given by the permittivities of the glass and metal ε_d = 1.5023^2=2.257, ε_{Au} = -104.5+ 3.68i at = 1550 nm, which results in the SPP wavelength λ_0 at 1567 nm. By applying a current of 200mA, a shift of 5 nm of the SPP wavelength is attributed to the change of refractive index of the glass Δn=0.0043 calculated by Equation 2.1 and Equation 2.2, indicating that the glass substrate was heated up to approximately 540 ˚C if the thermo-optic coefficient is given by dn/dT=7.9×10^{-6}˚C [29]. Two-dimensional (2-D) heat transfer of the system was simulated by Comsol 3.5, which indicated that the substrate was heated to 595 ˚C. The 2-D simulation results in greater temperature due to the assumption that the metallic slab has infinitely length. Taking a resistivity of 6.6

μΩ·cm, which is 3× as bulk ρ_{Au} = 2.2 μΩ ·cm, the resistance of the photonic crystal slab region is determined to be about 0.74 Ω [30]. The effective power dissipation of the plasmonic device is around 30 mW. While current was increased to 250 mA, the metallic grating was significantly overheated in the localized area.

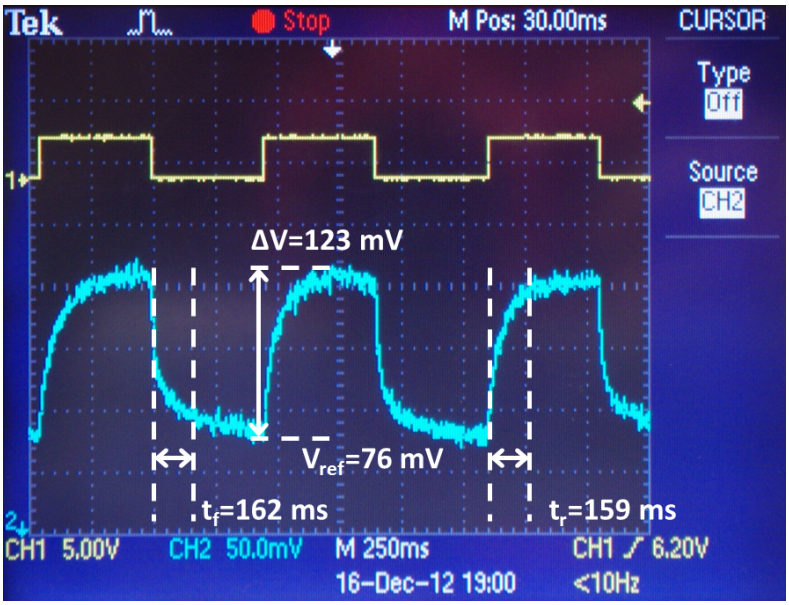

Figure 2.6: Thermo-optic modulation of the plasmonic bandgap: upper curve is the driving electric signal, and the lower curve is the responding optical signal.

Thermo-optic modulation was characterized using a probing wavelength at 1550nm from a tunable laser. The transmitted signal was measured with an InGaAs photodetector, whose photocurrent was then monitored by an oscilloscope. The device was driven by a square wave (0-3.2V) from a function generator operating at 1.09 kHz, corresponding to heating currents from 0 to 200

mA. The electric driving signals and the responding optical signals are shown in Figure 2.6, with modulation depth (defined as the induced change in the transmitted optical power normalized to the unperturbed optical output) exceeding 60%. The rising time and falling times were measured to be 159ms and 162ms respectively. This relatively low modulation speed is due to the slow thermal diffusion rate of the glass substrate.

2.3. Summary

In conclusion, we have demonstrated that the plasmonic bandgap of a metallic photonic crystal slab can be efficiently modulated by thermo-optic effects of a conventional glass substrate. This active control of plasmonic resonance is achieved by engineering the Fano resonance of the metallic photonic crystals to generate a sharp transitional edge. With only a moderate index modulation of 0.0043, we can achieve more than 60% modulation depth using surface-normal optical incidence. The power dissipation of the thermo-optic device is around 30mW, which is majorly limited by the small thermo-optic coefficient of the Corning glass substrate. We can still see that the sharpness of the transitional edge is not as perfect as that of the numerical simulation, which is possibly due to the fabrication variation and beam collimation. Further improvement to obtain an even sharper transitional edge will enable surface-normal electro-optic modulators using $LiNbO_3$ or nonlinear polymers as the substrates for high-speed modulation with even smaller index perturbation ($\Delta n \sim 0.001$). Such surface-normal plasmonic modulator can be easily expanded into arrayed structure. When integrated with

vertical-surface emitting laser array, it will provide enormous modulation bandwidth for board level optical interconnects and millimeter-wave photonic systems.

Reference

[1] T. Ebbesen, H. Lezec, H. Ghaemi, T. Thio, and P. Wolff, “Extraordinary optical transmission through sub-wavelength hole arrays,” Nature, 391, 667-669 (1998).

[2] J. A. Porto, F. J. García-Vidal, and J. B. Pendry, "Transmission resonances on metallic gratings with very narrow slits," Phys. Rev. Lett., 83, 2845-2848 (1999).

[3] H. J. Lezec, A. Degiron, E. Devaux, R. A. Linke, L. Martin-Moreno, F. J. Garcia-Vidal, and T. W. Ebbesen. “Beaming light from a subwavelength aperture,” Science, 297, 820-822(2002).

[4] J. G. Fleming, S. Y. Lin, I. El-Kady, R. Biswas and K. M. Ho, "All-metallic three-dimensional photonic crystals with a large infrared bandgap," Nature, 417, 52-55 (2002).

[5] B. Luk'yanchuk, N. I. Zheludev, S. A. Maier, N. J. Halas, P. Nordlander, H. Giessen & C. T. Chong, "The Fano resonance in plasmonic nanostructures and metamaterials," Nat. Mater., 9, 707-715 (2010).

[6] A. Christ, S.G. Tikhodeev, N. A. Gippius, J. Kuhl and H. Giessen, "Waveguide-plasmon polaritons: Strong coupling of photonic and electronic

resonances in a metallic photonic crystal slab," Phys. Rev. Lett., 91, 183901 (2003).

[7] L. Martín-Moreno, F. J. García-Vidal, H. J. Lezec, K. M. Pellerin, T. Thio, J. B. Pendry and T. W. Ebbesen, "Theory of extraordinary optical transmission through subwavelength hole arrays," Phys. Rev. Lett., 86, 1114-1117 (2001)

[8] G. D'Aguanno, N. Mattiucci, M. J. Bloemer, D. de Ceglia, M. A. Vincenti and A. Alu, "Transmission resonances in plasmonic metallic gratings," J. Opt. Soc. Am., B, 28, 253-264 (2011).

[9] A. Christ, T. Zentgraf, J. Kuhl, S. G. Tikhodeev, N. A. Gippius and H. Giessen, "Optical properties of planar metallic photonic crystal structures: experiment and theory," Phy. Rev. B, 70, 125113 (2004)

[10] J. M. Steele, C. E. Moran, A. Lee, C. M. Aguirre and N. J. Halas, "Metallodielectric gratings with subwavelength slots: optical properties," Phys. Rev. B, 68, 205103 (2003).

[11] A. Rahman, A. T. M., Peter Majewski and K. Vasilev, "Extraordinary optical transmission: coupling of the Wood-Rayleigh anomaly and the Fabry-Perot resonance," Opt. Lett., 37, 1742-1744(2012).

[12] J. M. McMahon, J. Henzie, T. W. Odom, G. C. Schatz and S. K. Gray, "Tailoring the sensing capabilities of nanohole arrays in gold films with Rayleigh anomaly-surface plasmon polaritons," Opt. Exp., 15,18119-18129(2007).

[13] S.-H. Chang, S. Gray, and G. Schatz, "Surface plasmon generation and light transmission by isolated nanoholes and arrays of nanoholes in thin metal films." Opt. Exp., 13, 3150-3165 (2005).

[14] R. W. Wood, “On a remarkable case of uneven distribution of light in a diffraction grating spectrum.” Philos. Mag., 4, 269–275 (1902).

[15] L. Rayleigh, “Note on the remarkable case of diffraction spectra described by Prof. Wood,” Philos. Mag., 14, 60–65 (1907).

[16] U. Fano, “The theory of anomalous diffraction gratings and of quasi-stationary waves on metallic surfaces (Sommerfeld’s waves).” J. Opt. Soc. Am., 31, 213–222 (1941).

[17] M. C-Y. Huang, Y. Zhou and C. J. Chang-Hasnain, "A surface-emitting laser incorporating a high-index-contrast subwavelength grating," Nature Photon., 1, 119-122 (2007).

[18] C. J. Chang-Hasnain, "High-contrast gratings as a new platform for integrated optoelectronics," Semicond. Sci. Technol., 26, 014043 (2011).

[19] D. M. Natarov, V. O. Byelobrov, R. Sauleau, T. M. Benson and A. I. Nosich, "Periodicity-induced effects in the scattering and absorption of light by infinite and finite gratings of circular silver nanowires," Opt. Express, 19, 22176-22190 (2011).

[20] N. P. Stognii and N. K. Sakhnenko, "Plasmon resonances and their quality factors in a finite linear chain of coupled metal wires." IEEE J. Sel. Top. Quantum Electron., 19, 4602207 (2013).

[21] J. M. Bendickson, E. N. Glytsis, T. K. Gaylord and D. L. Brundrett,"Guided-mode resonant subwavelength gratings: effects of finite beams and finite gratings," J. Opt. Soc. Am. A, 18, 1912-1928(2001).

[22] R. R. Boye and R. K. Kostuk, "Investigation of the effect of finite grating size on the performance of guided-mode resonance filters," Appl. Opt., 39, 3649-3653 (2000).

[23] J. Saarinen, E. Noponen and J. P. Turunen, "Guided-mode resonance filters of finite aperture," Opt. Eng., 34, 2560-2566(1995).

[24] J. Y. Suh, E. U. Donev, R. Lopez, L. C. Feldman, and R. F. Haglund, “Modulated optical transmission of subwavelength hole arrays in metal-VO2 films,” Appl. Phys. Lett., 88, 133115 (2006)

[25] D. Nau, R. P. Bertram, K. Buse, T. Zentgraf, J. Kuhl, S. G. Tikhodeev, N. A. Gippius and H. Giessen, “Optical switching in metallic photonic crystal slabs with photoaddressable polymers,” Appl. Phys. B, 82, 543-547 (2006)

[26] T. Nikolajsen, K. Leosson and S. I. Bozhevolnyi, “Surface plasmon polariton based modulators and switches operating at telecom wavelengths,” Appl. Phys. Lett., 65, 5833-5836 (2004)

[27] J. Z. Xin, K. C. Hui, K. Wang, H. L. W. Chan, D. H. C. Ong and C. W. Leung, “Thermal tuning of surface plasmon resonance: Ag gratings on barium strontium titanate films,” Appl. Phys. A, 107, 101-107 (2012)

[28] H. R. Raether, Surface plasmons on smooth surfaces and Rough Surfaces (Springer, 1988).

[29] J. Wray and J. T. Neu, "Refractive index of several glasses as a function of wavelength and temperature," J. Opt. Soc. Am., 59, 774-776, (1969).

[30] M. Ordal, L. Long, R. Bell, S. Bell, R. Bell, R. Alexander and C. Ward, "Optical properties of the metals Al, Co, Cu, Au, Fe, Pb, Ni, Pd, Pt, Ag, Ti, and W in the infrared and far infrared." Appl. Optics, 22, 1099-1119 (1983).

[31] M. Hong, A. K-Y Jen and L. R. Dalton. "Polymer-based optical waveguides: materials, processing, and devices." Adv. Mater., 14, 1339-1365 (2002).

CHAPTER 3. ELECTRO-OPTIC MODULATORS BASED ON HYBRID POLYMER-PLASMONIC STRUCTURES

High-speed electro-optic (E-O) modulators have been identified as the key components for communication systems. Such modulators allow large information bandwidths with zero-chirp or adjustable-chirp operation, which have widely been used in high-speed optical fiber transmission systems [1-4]. In this chapter, we show the demonstration of electro-optic modulation using hybrid polymer and plasmonic structures. We design two structures for E-O modulation in this chapter. The first device is based on Indium-Tin Oxide (ITO)/polymer/plasmonic structure, which shows efficient modulation due to large poling area. We also design an in-plane modulation structure with interdigitated configuration, which is expected to operate at ultra-high speed and can be integrated with other optoelectronic devices for free-space 3-D optical interconnects.

3.1. Overview of Polymer-based Electro-Optic Modulators

E-O modulators are based on the Pockels effect in a medium. The refractive index $n(E)$ of a material can be written as a function of the applied electric field E. The refractive index can be express as [5]

$$n(E) = n + a_1 E + a_2 E^2 + \ldots \tag{3.1}$$

Here a_1 and a_2 are linear and second-order coefficients, respectively. The Pockels effect measures the linear electro-optic coefficient picometers of displacement of the wavelength per volt of applied field. The Pockels effect can be written in [5]

$$\Delta n = -\frac{1}{2} r_{ij} n^3 E \tag{3.2}$$

where Δn is the modulated refractive index by Pockels effect and r_{ij} is the Pockels coefficient. Crystals and materials lacking a center of symmetry are noncentrosymmetric and exhibit a linear E-O effect. Lithium niobate ($LiNbO_3$), potassium dihydrogen phosphate (KDP), and gallium arsenide (GaAs) are materials commonly used for E-O systems [6-12]. Current focus for researchers is developing E-O materials that meet requirements such as large nonlinear susceptibility, low optical loss, fast response time, high optical damage threshold, and cost-effectiveness to integrate with other materials in the systems [14-16]. Among different material choices, polymers have been identified as one of the most promising candidates that meet the above requirements for the development of E-O modulators [17-20]. Polymers with E-O properties have been under investigation for several years. Compared to conventional inorganic materials, organic E-O materials provide advantages such as large E-O coefficient (larger than 300 pm/V), low dispersion in the index of refraction from infrared to millimeterwave, ultrafast response time (femtoseconds), easily integrated with other materials and substrates, and low-cost in the system. Recent advances in

polymeric E-O materials and device fabrication techniques have significantly benefit photonic technologies and increased the potential for incorporation of these materials into modern high bandwidth telecommunication and information processing systems [21-28].

3.1.1. Large Pockels Coefficient Through Poling Process

The key step to create large Pockels effect in organic E-O materials is generating noncentrosymmetric order of nonlinear optical chromophores through electric field poling method. Advanced poling techniques have been investigated during the past, such as contact poling, pulse poling and pyroelectric poling [29-31].

Figure 3.1 shows the mechanism for standard contact poling of polymer sandwiched between top Au and bottom ITO layers, which are typically used as electrodes. Before poling the chromophores with a permanent dipole moment are randomly oriented. During the poling process, the sample was heated to the glass transition temperature (T_g=120°C) of the polymer in the presence of a 100 V/μm electric field. At the glass transition temperature, the chromophore molecules are free to move and become partially aligned. When reaching the glass transition temperature, the Au/polymer/ITO device was then cooled down to room temperature, and the poling voltage was turned off upon reaching room temperature. Through this poling process, the aligned molecules of the NLO-chromophore are frozen and E-O effect in the film is created. Leakage current

during poling is monitored in situ as shown in Figure 3.2. The poled area with the electrode is around 12 mm^2 and the polymer thickness is 1 μm.

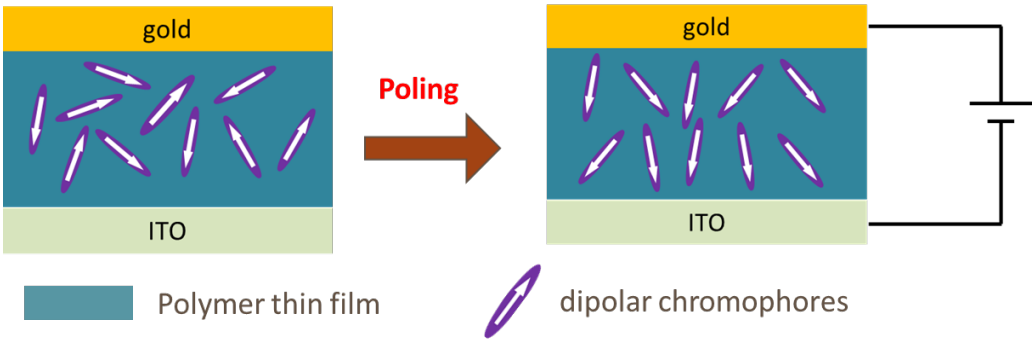

Figure 3.1: Mechanism for standard contact poling of polymer sandwiched between top Au and bottom Indium-Tin Oxide layers.

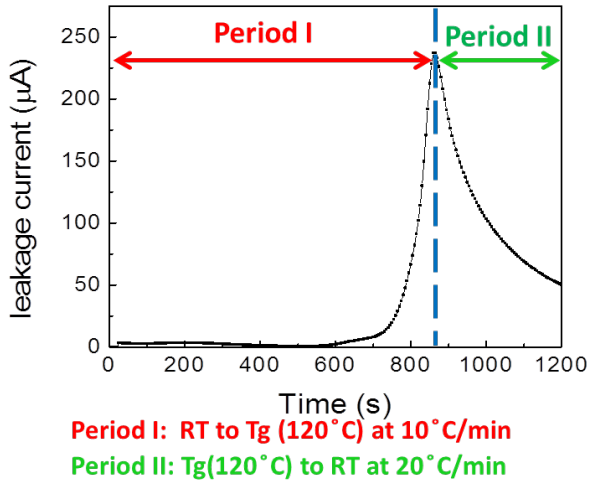

Figure 3.2: Leakage current during poling is monitored in situ.

E-O Coefficient was measured by standard Teng-man method [32]. This is a simple and effective method to evaluate poling efficiency, as shown in Figure 3.3.

After poling the sample shows birefringence, which indicates that the refractive indices depend on the polarization and propagation direction of light. A single wavelength laser was used to characterize the E-O coefficient. The s and p polarized lights at 1550 nm are in phase after passing through a linear polarizer, which are incident to the sample with a 45° angle. After propagating within the material and being reflected by the Au surface, the phase retardation can be analyzed and detected by an InGaAs detector. A driving AC voltage applied to the device from the function generator gives a modulation of the phase retardation. The modulation amplitude is proportional to the E-O efficiency of the material and could be measured using in lock-in amplifier.

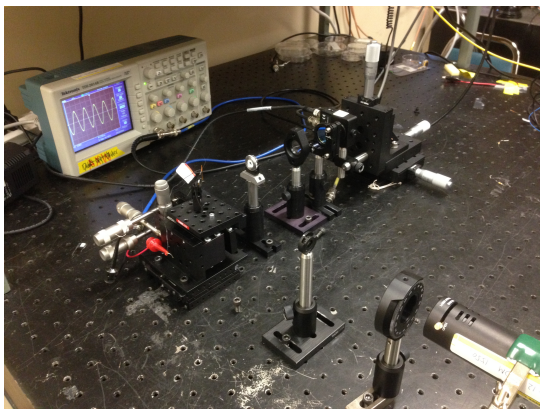

Figure 3.3: E-O Coefficient was measured by standard Teng-man method.

Poling process is a critical issue for E-O polymer photonic devices, especially for nanophotonic devices. Solution-based organic materials have been identified as one of the most promising active materials to be infiltrated into

various nanostructures. Among all the nanophotonic modulators, slot waveguides infiltrated by E-O polymer are the most common type of structures that attract the most research interests [33-34]. The poling efficiency of E-O polymer decreases when the slit becomes narrower due to the significant increase in charge injection. Due to the degradation in poling efficiency, significant challenges still exist in the integration of high-efficient nonlinear polymers into silicon nanophotonic devices such as slotted waveguides and photonic crystals.

3.1.2. Silicon-Organic Hybrid Modulators

Silicon photonics are expected to be one of the potential platforms of interconnect technology due to its electronics integration capability, mature manufacturing infrastructure, and price volume curve [35]. However, silicon does not have Pockels effect due to its centrosymmetry in crystal lattice. Silicon-polymer hybrid waveguide modulators have been widely investigated and expected to be important components in integrated photonics systems.

In hybrid E-O polymer silicon systems, passive components are fabricated in silicon to form nanoscale slotted waveguides, which commonly in configurations of micro-rings, striplines or combine with photonic crystals [36-45]. Silicon polymer hybrid slot waveguides show a path to significantly high bandwidth operation of over 100 GHz [46-48]. High-speed strip-loaded slot waveguide modulators based on slicon technology have been demonstrated [40]. The measured frequency response of the modulator was found to be about 100

GHz (at 3-dB signal strength) figure of merit of $V_\pi L = 11$ V·mm. A single-carrier data rate of 112 Gbps based on this structure is observed through 16 quadrature amplitude modulation.

The high index contrast between silicon and E-O polymer filled in the gap enables extremely compact waveguides with high mode field concentrations. The large fraction of the guided mode into the gap within the center of a silicon waveguide magnifies the electric field associated with the optical mode. A linear E-O response and pure phase modulation can therefore be introduced by filling the gap with poled E-O polymers. One major challenge is low in-device poling efficiency, which could be one order lower than the optimum value reported in thin film devices using the same material. Improved poling efficiency in slot waveguide can be achieved by depositing a thin Titanium Dioxide (TiO_2) layer (~5 nm) to reduce charge injection [49].

3.1.3. Polymer-Plasmonic Hybrid Modulators

Silicon modulators have been demonstrated with merits of large RF bandwidth using a travelling wave modulator, compactness using a photonic-crystal modulator and the energy efficiency using a ring modulator [50-54]. The plasmonic-organic phase modulator (PPM) has been investigated during the past. Such plasmonic-organic hybrid modulator shows supreme advantages compared with silicon-based devices, and it could combine the advantages of the aforementioned modulators [55-58]. Using gap SPPs, it is possible to design

passive and active components with ultra-compact dimensions. Furthermore, the uses of the Pockels effect in organic materials avoid the speed limitation associated with the carrier lifetime in plasma-effect-based injection-type modulators. The high conductivity of the metal films and the small capacitance of the device result in an ultra-small resistance-capacitance (RC) delay, which does not show any practical speed limitation.

Figure 3.3 shows the plasmonic phase modulator, which consists of two metal electrodes separated horizontally by a nanoscale slot. The slot is filled with a nonlinear organic material, and the refractive index of the polymer can be changed by applying a static electric field. With an electro-optic coefficient r_{33}, the change in the refractive index can be calculated using Equation 3.3. By introducing an index perturbation of the polymer in the slot waveguide, the digital information is encoded in the phase of the SPP. Light is coupled into plasmonic waveguide from a silicon tapered coupler. At the end of the modulator section, the SPP is back-converted into a photonic mode. The modulator exhibits a flat modulation frequency response up to at least 65 GHz, with a device length of only 29 μm and energy consumption of 60 fJ bit^{-1}.

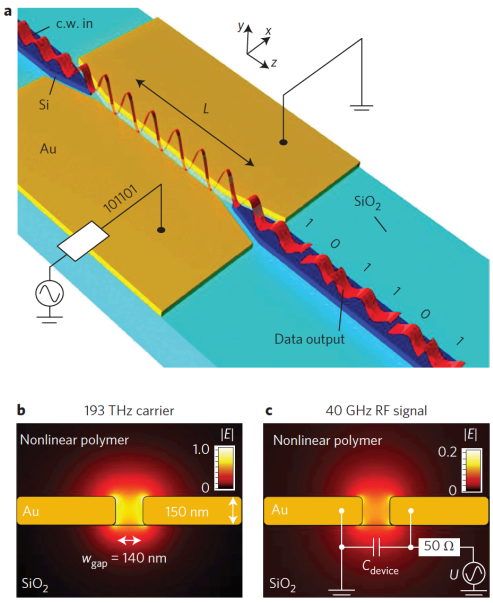

Figure 3.3: Schematic of a high-speed plasmonic phase modulator, reprinted with permission from [55]. The phase of the SPP excited within the metal slots is changed by applying a modulating voltage. The bottom figures show mode profiles of the SPP and RF signals.

An all-plasmonic Mach-Zehnder modulator (MZM) was investigated as a novel photonic integrated circuit that shows advantages in footprint, speed and energy consumption compared with state-of-the-art silicon MZMs [56]. In Figure 3.4, an all-plasmonic MZM was fabricated by nanoscale patterning of a metallic waveguide, which has a length of only 10 μm. This is a record of small footprint for a MZM which consists of the phase-modulation section with the mode converter. This all-plasmonic MZM demonstrates high-speed operation up to 72 Gbit s^{-1} with a $V_{\pi}L$ of 60 V μm and energy consumption of 25 fJ bit^{-1}.

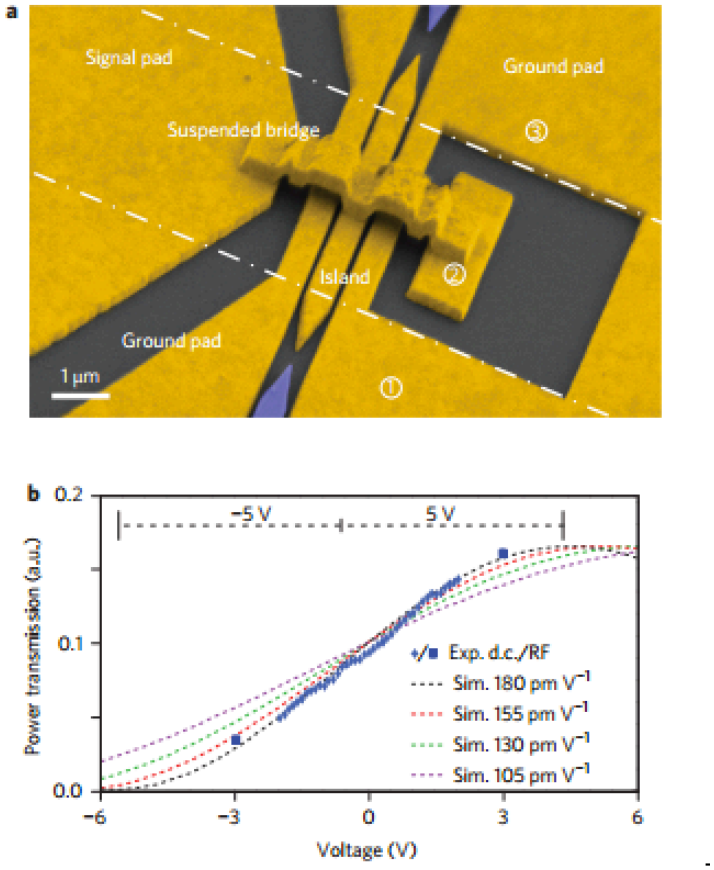

Figure 3.4: An all-plasmonic MZM by nanoscale patterning of a metallic waveguide, reprinted with permission from [56]. The bottom figure shows the measured electro-optic coefficient.

3.2. Modulation Based on ITO/Polymer/Plasmonic Sandwiched Structure

3.2.1. Theoretical Study

In our work, we designed, fabricated, and characterized a surface-normal plasmonic/polymer modulator that combines the merits of subwavelength metal gratings and efficiently poled E-O polymer thin film [59].

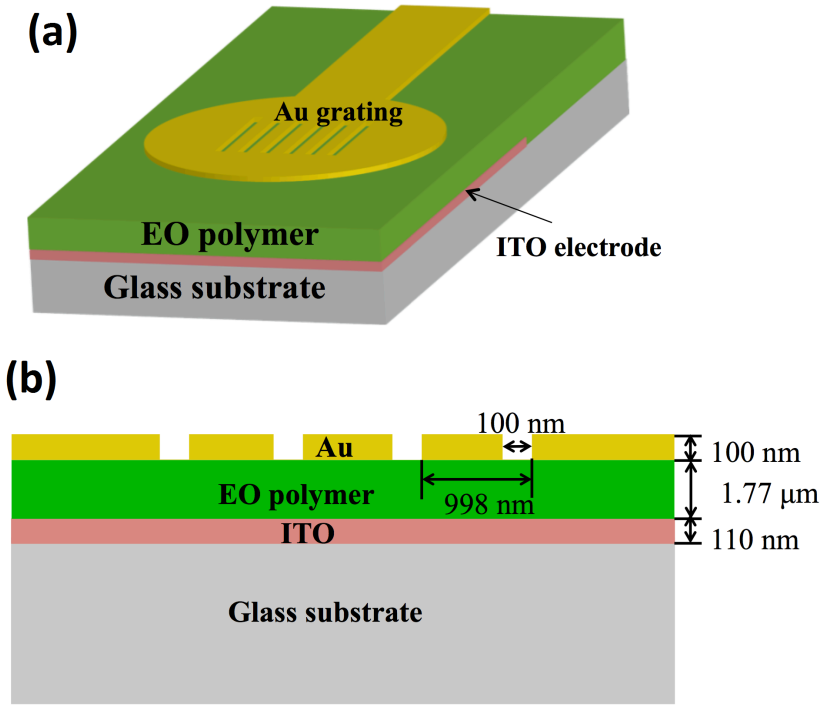

Figure 3.5: (a) Schematic illustration of the surface-normal plasmonic modulator; (b) cross-sectional view of the device structure with geometric parameters.

The configuration of the device is shown in Figure 3.5, which consists of a gold (Au) /polymer /ITO sandwich structure on a glass substrate. A layer of 110

nm ITO film was deposited onto a 25 mm×25 mm glass substrate using a two-inch ITO target (90% In_2O_3, 10% SnO_2 by weight) in an AJA Orion 5 sputtering system. Substrate rotation was employed to ensure uniform film thickness. Deposition was performed at 75 W of RF power and a chamber pressure of 5 mTorr using 9.7 sccm of argon and 0.3 sccm of oxygen. Substrates were heated to 300 °C during the deposition. The ITO film thickness was measured on photolithographically patterned features using a Tencor Alpha Step 500 profilometer. The resistivity was measured to be 334 μΩ·cm using a Jandel Multi Height Probe with a RM2 Resistivity Test Unit. The ITO electrode was patterned and partially etched by hydrochloric acid in order to reduce the capacitance with the Au grating. The E-O polymer in this study is a guest-host polymer composite in poly (methyl methacrylate-*co*-styrene) (PMMA-*co*-PS) using AJLZ53 as one of most efficient and photo-stable dipolar tetraene chromophores at the loading level of 15 wt%. This polymer exhibits large E-O coefficient and high processing reliability in poled thin films, and has been used as a standard EO polymer with glass transition temperature (T_g) of 110 °C for the study of photonic devices. Its thin film was prepared by spin-coating of formulated solution in dibromomethane onto the ITO substrate with a spin speed at 2000 rpm for 60 seconds, followed by overnight baking in vacuum oven at 65 °C to ensure complete removal of the residual solvent, leading to high optical quality films with thickness of 1.77 μm. The refractive index of the unpoled polymer films was measured by ellipsometry to be 1.571 at 1522 nm. A 100 nm Au thin film was deposited onto the polymer

layer by thermal evaporation with a deposition rate of 8 Å/sec. In order to reduce the RC delay of the device, a shadow mask was used to reduce the gold pad size. The key for enabling modulation is to create the Pockels effect in the E-O polymer sandwiched between the top Au and bottom ITO layers. This was achieved by generating the noncentrosymmetric order of nonlinear optical chromophores through poling process in presence of applied electric field. The E-O polymer was poled with contact poling method with E-O coefficient r_{33} of 71 pm/V as measured by the standard Teng-man reflective measurement system at 1300 nm. The nanoscale slits were milled by focused-ion beams (FIB), with gallium ion energy of 30 kV and current of 10 pA. The periodicity of the grating was designed at 978 nm with the slit width of 100 nm, as shown in Figure 3.5(b).

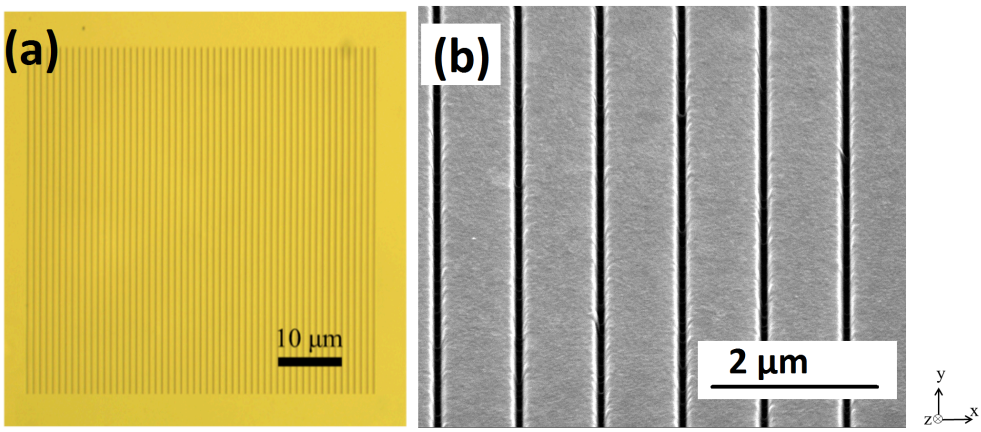

Figure 3.6: (a) Optical microscopy image of the fabricated device; (b) SEM image showing the fabricated subwavelength metal grating.

The key challenge faced in the fabrication process is precisely controlling geometrical dimensions and obtaining smooth slits at the Au/polymer interface.

The ability to control the width of the gap and to minimize the fabrication defects is crucial for obtaining a sharp bandgap for the device. An optical image of the fabricated 53.8 μm × 53.8 μm plasmonic grating structure after the FIB milling is shown in Figure 3.6(a). A high-resolution scanning electron microscopy (SEM) image of the grating is shown in Figure 3.6(b), which indicates the high quality of the grating structure with smooth slits in the presence of E-O polymer thin film.

3.2.2. Experimental Characterization

The Fano resonances in the subwavelength metal grating have been intensively investigated by many researchers, which has been discussed in the previous chapter. Figure 3.7(a) shows the experimental setup of measuring the transmission spectrum. A broadband continuous wave laser (Thorlabs, S1FC1550) centered at 1550 nm was coupled into a fiber-based polarizer (Thorlabs, ILP1550SM-FC) to generate a linearly transverse magnetic (TM) polarized light with electric field polarized perpendicular to the slit direction. The output light was then collimated through a 40× objective lens (NA=0.65). A 50 μm pinhole was used to block the excessive light of the collimated beam before coupling to the device in order to achieve maximum coupling efficiency to the SPP mode. The device was mounted on a five axis stage, which allowed precise adjustment of the position as well as the incident angle within 5×10^{-5} rad. The transmitted beam after the sample was focused by a 40× objective lens and coupled into an optical spectrum analyzer (Thorlabs, OSA203B) with a standard SMF-28 fiber.

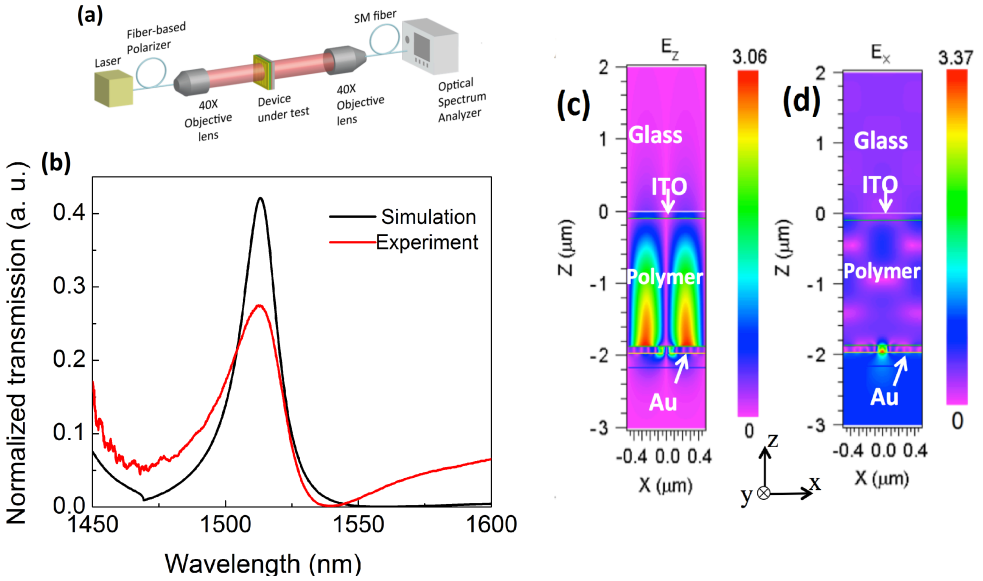

Figure 3.7: (a) Experimental setup for optical transmission spectrum; (b) The simulation and experimental curves showing the optical transmission spectrum; The electric field distribution along (c) z direction and (d) x direction at 1522 nm.

Figure 3.7 (b) shows the measured and simulated transmission spectra with a wavelength range from 1450 nm to 1600 nm. The simulation is based on Rigorous Coupled Wave Analysis (RCWA) in DiffractMod of Rsoft^{TM}. The transmission spectra, indicate the asymmetric lineshape of the Fano resonance with a sharp transition edge. The resonance is attributed to the coupling of the discrete guided modes induced by Bragg-grating-modulated SPPs with the Fabry-Perot resonance in the narrow slits and waveguide mode resonance in the polymer layer [59-60]. The location of the transmission maximum agrees with the simulated curve, as shown in Figure 3.7(b). The reduced peak intensity and

broadening of the spectrum are attributed to the non-perfect collimation and the fabrication defects of the grating. Figure 3.7(c) and Figure 3.7(d) show the cross-sectional views of the electric field distribution $|E/E_0|$ (where E_0 is the electric field amplitude of the incident light) associated with the SPPs at the Au-polymer interface at 1522 nm along the z-axis and x-axis, respectively with no applied voltage. The enhanced E_z extend into the polymer layer, as shown in Figure 3.7(c), resulting in overall 3× electric field amplitude enhancements over a large volume in the polymer layer, which has very good overlap with the modulating electric field induced by the vertical electrodes. Figure 3.7(d) indicates extraordinary transmission effects in the narrow slits.

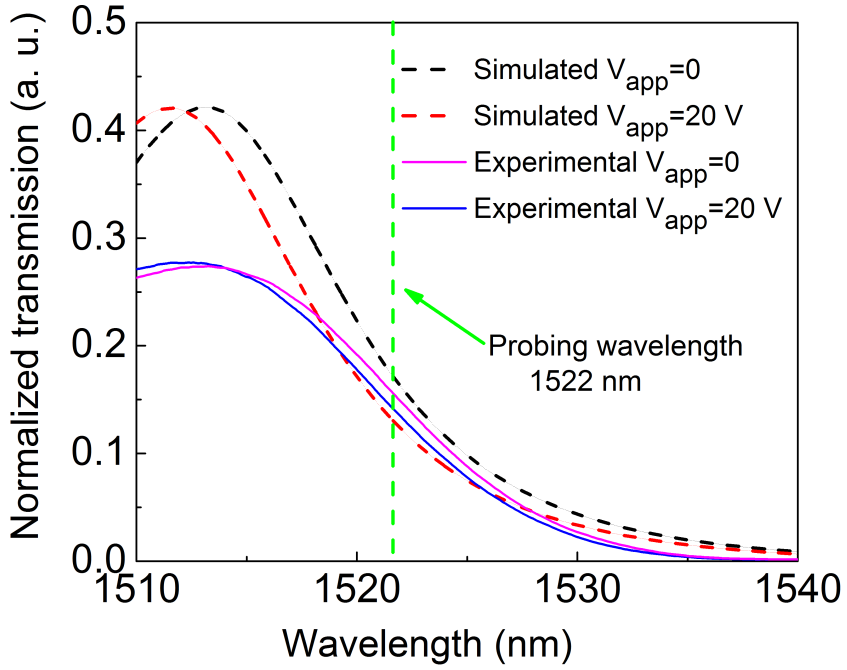

Figure 3.8: The simulation and experimental curves showing the spectrum shift under 20V voltage.

In order to investigate the E-O modulation due to the Pockels effect of the polymer layer, a 20V DC voltage was applied between the grating and the grounded ITO layer. The change of the refractive index Δn can be written as [5]

$$\Delta n = -\tfrac{1}{2} n_e^{\,3} r_{33} \frac{V}{d} \tag{3.3}$$

where V is the applied voltage and d is the polymer film thickness. The extraordinary refractive index n_e of the poled films is 1.61 measured by Metricon 2010 prism coupler. Considering the results that r_{33} is 71 pm/V at 1300 nm corresponds to 60 pm/V at 1522 nm based on the two-level approximation [30], Δn was calculated as 0.0014. The wavelength of the Fano resonance is determined by the periodicity of the structure p, Au permittivity ε_{Au}, and the polymer permittivity ε_d, which can be explained by the SPP zero-order relation [61]:

$$\lambda_0 = n_{spp} p \tag{3.4}$$

$$\text{where} \quad n_{spp} = \mathrm{Re}\left(\sqrt{\frac{\varepsilon_{Au}\varepsilon_d}{\varepsilon_{Au}+\varepsilon_d}}\right) \tag{3.5}$$

The simulation curves in Figure 3.8 indicate a wavelength shift occurs due to the small change of polymer index Δn of 0.0017 in the presence of the applied voltage. With a probing wavelength of 1522 nm, the simulated transmission spectra show that a very small index modulation of 0.0017 induces the decrease of the optical transmission from 17.5% to 12.6%. Figure 3.8 also shows experimental results of the wavelength shift with an external 20V voltage applied.

The measurement curves show that the optical transmission drops from 15.3% to 14.1% at 1522 nm. The discrepancy between the experiment and simulation possibly result from the degradation of the polymer E-O efficiency r_{33} in the grating region after the FIB process. Due to the small thermal conductivity of polymers [62], FIB heating could induce thermal relaxation of poled films to certain extend, and therefore the r_{33} value of the grating region (53.8 μm×53.8 μm) is degraded compared to the measured value using the Teng-man method with a large collimated beam size (2.6 mm ×2.6 mm). Thin film E-O measurement proves that poled films, after being exposed to thermal excursion at 60 °C for 15 minutes, retains about 70% of its initial r_{33} values. From the experimental result of wavelength shift in Figure 3.8, the change of the refractive index was estimated to be 0.00063, which results in an in-device r_{33} of 27 pm/V at 1522 nm based on Equation 3.3. The change of the optical field distribution at the probing wavelength induced by the modulation of the dielectric layer refractive index can be found in our previous work in chapter 2.

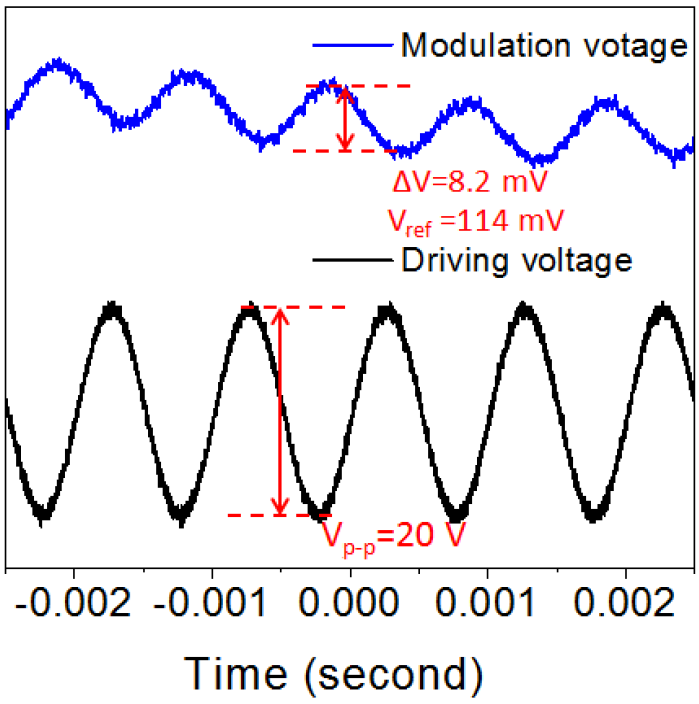

Figure 3.9: Electro-optical modulation of the Fano resonance: lower curve is the driving electric signal, and upper curve is the responding optical signal.

A tunable laser (HP 8168A) at 1522 nm was used in order to characterize the E-O modulation. An InGaAs photodetector was connected to an oscilloscope in order to monitor the transmitted optical power. A 1 kHz sinusoidal wave (20V peak-to-peak) was applied to the device from a function generator (Wavetek, Model 395). The output of the optical signal in response to the electric driving signal is shown in Figure 3.9. The modulation depth, which is the amplitude of the modulation voltage divided by the reference signal, only achieves 7.2% in our experiment, however, it is highly possible to obtain large E-O modulation (>50%)

by using more efficient (r_{33} > 200 pm/V) E-O polymers with higher thermal stabilities. Future work will also be focused on optimizing the FIB fabrication condition to obtain sharper transition edge of the Fano Resonance, which will increase the modulation depth. Modulation with lower driving voltage can be achieved by decreasing the thickness of the E-O polymer layer [63]. By these optimizations in design and fabrication, it would be possible to reduce the driving voltage to ~1V and achieve a modulation depth of ~3dB.

3.3. Modulation Using Polymer in Interdigitated Metallic Slits

3.3.1. Theoretical Investigation

The schematic illustration of the device is shown in Figure 3.10(a), which consists of a nanoscale interdigitated structure with electrical contacting pads on a quartz substrate with an index of 1.45. To modulate the optical transmission, a thin layer of E-O polymer is placed on top of the gold (Au) interdigitated structure, which could also infiltrate into the subwavelength slits. The applied modulating voltage to the electrodes will induce alternatively reversed voltage polarity across each adjacent pair of the Au fingers. Such voltage will result in an index perturbation within the polymer layer, and the 1 and 0 signals are encoded in the intensity of optical transmission, which are in response with the applied electric signal. The Au film thickness is 50 nm, the grating period is 1020 nm and the gap width is 200 nm, as shown in the cross-sectional view in Figure 3.10(b). The thickness of the E-O polymer is 650 nm with an index of 1.57 at the operating

wavelengths. When a transverse magnetic (TM) plane wave with a broadband spectrum is surface-normally incident to the device, Fano resonance will be excited, which manifests itself as an asymmetric spectrum with a sharp plasmonic bandgap. The optical transmission of the periodic structure in Figure 3.10(a) is simulated based on Rigorous Coupled Wave Analysis (RCWA). At the near infrared wavelength range from 1510 nm to 1620 nm, we can clearly observe the resonance, which is due to the coupling between the grating-modulated SPPs at metal/polymer interface and the waveguide resonance in the polymer layer. The interaction of the waveguide resonance in the polymer layer, which possesses a broadband nature, and the SPPs within the polymer leads to extraordinary optical transmission with narrow spectral features at the specific wavelength, as shown in Figure 3.11(a).

The optical transmission spectra of the metallic photonic crystals were simulated with index modulation of the polymer layer of 0, -0.005 and -0.01, respectively. Figure 3.11(a) shows that decreasing the refractive index of the polymer will induce the blue-shift of the transmission spectrum. With a probing wavelength of 1565 nm, the simulated optical intensity distribution suggests that an index modulation of -0.01 will cut off the resonant mode in the metal slits, giving an optical transmission change from 53% to 12%. Figure 3.11(b) and Figure 3.11(c) show the cross-sectional views of the electromagnetic field distribution $\left| E/E_0 \right|$ (where E_0 is the electric field amplitude of the incident light), associated with the SPPs at the Au-polymer interface at the peak of the resonance

along the z-axis and x-axis respectively without biased voltage from the electrodes. The enhanced E_z extend into the polymer layer, as shown in Figure 3.11(c), has very good overlap with the modulating electric field induced by the coplanar electrodes.

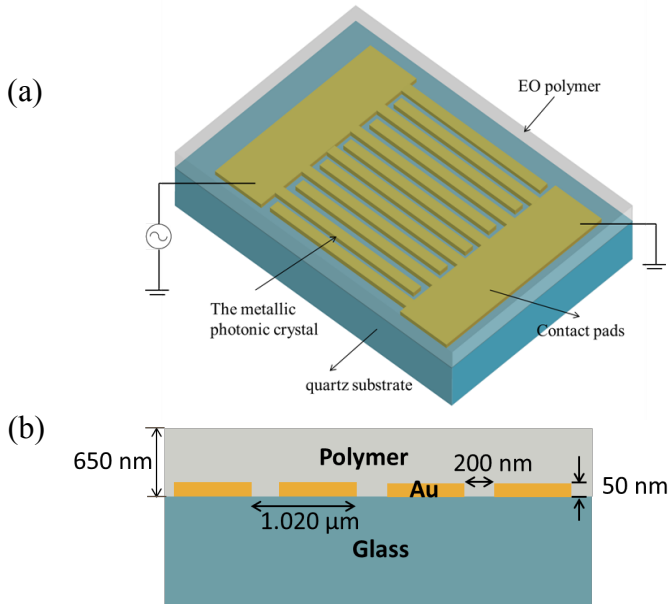

Figure 3.10: (a) Schematic illustration of the proposed coplanar interdigitated structure; (b) cross sectional view with geometrical parameters.

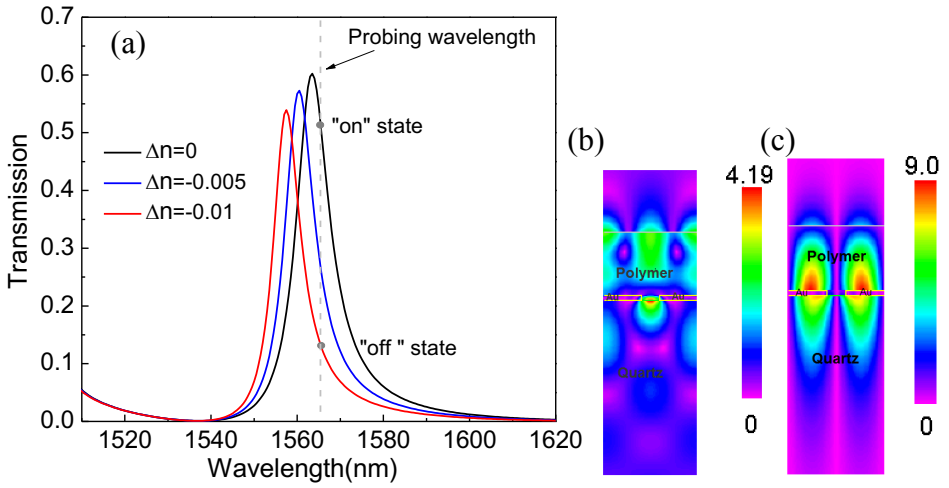

Figure 3.11: (a) Simulated optical transmission of the structure at the near infrared wavelength with on and off states; (b) electric field distribution of the structure along x axis; (c) electric field distribution of the structure along z axis.

3.3.2. Experimental Characterization

The nanoscale interdigitated structure was fabricated using focused ion beam (FIB) lithography, which could precisely control the period of the structure and the gap width. The nanoscale slits were milled by ion beams, with gallium ion energy of 30 kV and current of 50 pA. Figure 3.12(a) shows the fabricated device with area of 30μm×50μm. A SEM image of the nanoscale structure is shown in Figure 3.12(b), which indicates the fabricated ultra-smooth slits with width of 200 nm. The E-O polymer in this study is a guest-host polymer composite in poly (methyl methacrylate-co-styrene) (PMMA-co-PS) using AJCK-L1 chromophore at the loading level of 20 wt%. This polymer exhibits large E-O coefficient with good thermal reliability in poled thin films, and has been used as a standard EO

polymer with glass transition temperature (T_g) of 120 °C. The polymer thin film layer was prepared by spin-coating of formulated solution in dibromomethane onto the Au interdigitated structure. The film thickness was 750 nm with a spin speed at 2000 rpm for 60 seconds, followed by baking in vacuum oven at 65 °C overnight to remove of the residual solvent.

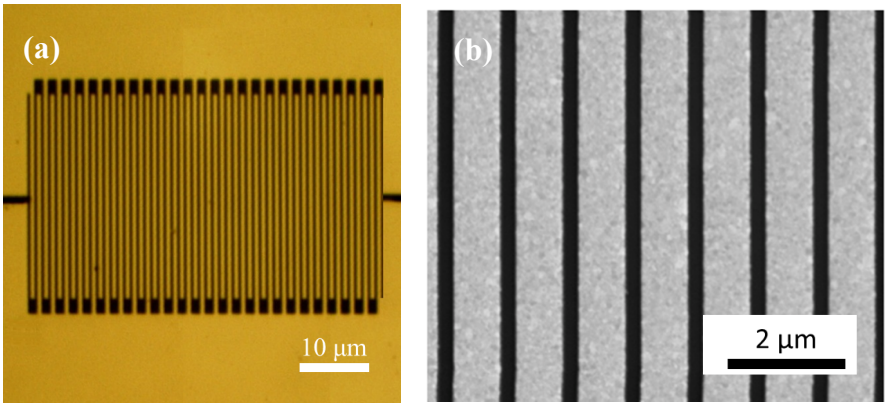

Figure 3.12: (a) A microscope image of the device structure; (b) high-resolution SEM image shows the fabricated slits.

The E-O polymer was poled with contact poling method when a high electric field was applied at the two Au electrodes. The key for enabling modulation is to create electro-optic effect in the E-O polymer layer. This was achieved by generating the noncentrosymmetric order of nonlinear optical chromophores through poling process in presence of applied electric field. During the poling process, the sample was heated to the glass transition temperature of the guest/host polymer, and a 25 V voltage was applied at each Au electrodes. When the sample temperature reached the glass transition temperature, the chromophore molecules were free to move and the dipoles could be aligned with

poling field. Therefore, symmetry was broken during this process. Upon reaching the glass transition temperature, the sample was then cooled down to room temperature and the aligned molecules of the NLO-chromophore were frozen during the process. Finally, the poling voltage was turned off when the sample reached room temperature and E-O effect in the slot region is created through this poling process. Leakage current during poling is monitored in situ and is plotted in Figure 3.13 It can be seen that the leakage current reached maximum at the glass transition temperature, and dropped rapidly when the sample was cooled down.

Figure 3.14 shows the optical transmission spectrum of the device. In the experiment, a broadband light source with wavelength range of 1500-1600 nm was coupled into a single-mode polarization-maintaining (PM) fiber with an in-line fiber polarizer, resulting in TM polarized light that is along the grating wave vector. The output light was collimated by a 40× objective lens (NA=0.65). The sample was mounted on a five-dimensional translation/rotation stage, allowing highly precise spatial alignment and angular adjustment with respect to the collimated beam. The transmitted beam after the sample was focused by another 40× objective lens, which was then coupled into a standard SMF-28 fiber and measured by a HP 70951A optical spectrum analyzer. The measured transmission spectrum is shown in Figure 3.14 with full width half maximum of ~30nm, which is much larger compared with the simulation results (11 nm) in Figure 3.11(a). The broadening of the resonance and large edge of the plasmonic bandgap is due

to the non-perfection of the beam collimation of the incident beam and fabrication defects. In addition, the device has a finite size and the broadening of the resonance is observed when further shrinking the device size. Moreover, thermally evaporated Au film shows higher imaginary part of the dielectric permittivity than bulk Au adopted in the simulation, which further reduce the sharpness of the edge that is adopted in the modulation.

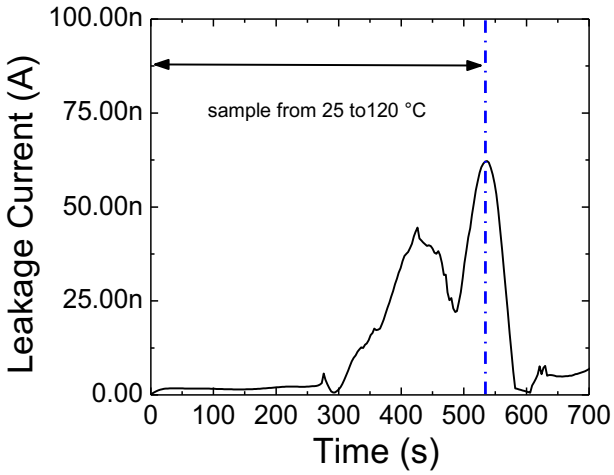

Figure 3.13: Leakage current during the poling process.

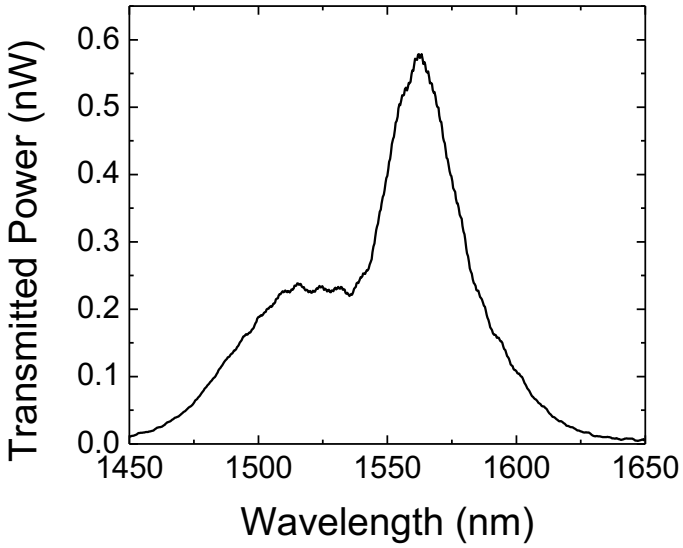

Figure 3.14: Transmission spectrum of the structure.

From the transmission spectrum, it can be predicted that the maximum intensity change should be observed at wavelength which shows half maximum intensity of the resonance peak. A tunable laser (HP 8168A) at 1565 nm was used in order to characterize the E-O modulation. An InGaAs photodetector was connected to an oscilloscope in order to monitor the transmitted optical power. A 2.5 kHz sinusoidal wave V_{pp1} with 10 V peak-to-peak amplitude was applied to the device from a function generator (Wavetek, Model 395). Therefore, the transmission intensity change could be represented as the voltage output when an external driving voltage was applied to the device. The transfer function, which shows output of the optical signal in response to the electric driving signal, is shown in Figure 3.15.

When applying a voltage, the electrical fields are mainly distributed within the slit and on the top surface of the gold, and the field intensity decays exponentially within the polymer. In a thin film sandwich structure based on ITO/polymer/Au configuration, the polymer thin film could achieve a r_{33} value around 120 pm/V due to the uniform distribution of the electric field during poling and modulation. Our in-device r_{33} is much lower, which is mainly limited by the non-uniform electric field within polymer layer. In addition, such coplanar fingered structure shows a much higher leakage current density during poling process compared with ITO/polymer/Au sandwich structure due to the electric discharge effect at the sharp tips. This leads severe charge injection leakage and further degrades the poling efficiency. Future investigation could be focused on improving poling efficiency using a buffer layer to prevent charge injection, such as a Titanium dioxide thin layer of 5 nm. In modulation experiment, The V_{pp2} in Figure 3.15 is 1.5 mV measured using an oscilloscope and modulation was observed up to 15 MHz using a microwave spectrum analyzer, which is limited by the TIA impedance detector. Although only a small modulation depth of 1.5% was achieved, such coplanar structure with ultra-compact footprint is expected to operate at high speed >1 GHz.

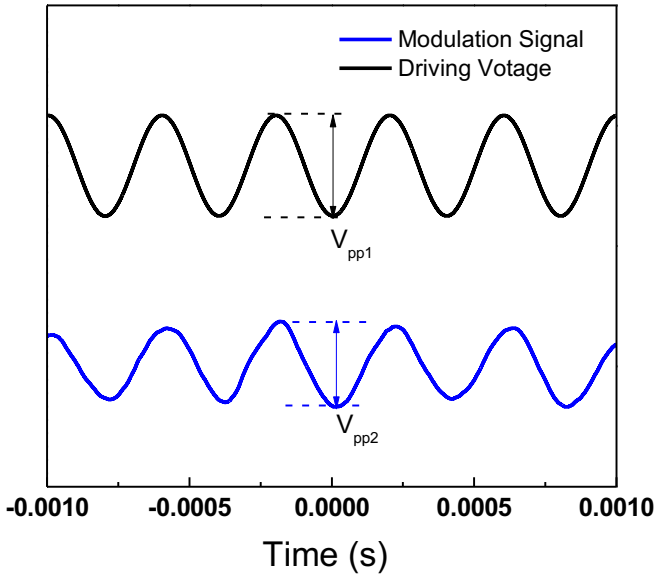

Figure 3.15: The electro-optic modulation response of the device.

3.4. Summary

In this chapter, we have reviewed polymer-based E-O modulators for high-speed communication system. Compared with silicon-based devices, plasmonic-organic hybrid structures show several advantages including compact footprint, large RF bandwidth and small power consumption. Due to the extraordinary transmission, the hybrid plasmonic-polymer device exhibits a Fano resonance with a sharp transition edge. The E-O effect in the polymer film enables modulation of the Fano resonance.

Surface-normal modulators are based on the extraordinary transmission of the subwavelength plasmonic grating and the efficiently poled E-O polymer thin

film, which provide out-of-plane photon manipulation with high optical confinement and low insertion loss. We demonstrated two surface-normal modulation devices based on electro-optic polymer with metallic photonic crystals.

The first device is based on ITO/polymer/plasmonic structure. Such structure shows efficient modulation due to large poling area. The sandwich structure shows the disadvantage of large capacitance, which limits the operation speed of the modulator. We also designed a free-space coupled plasmonic modulator based on interdigitated configuration, which is expected to be operated at ultra-high speed and can be integrated with other optoelectronic devices for free-space 3-D optical interconnects.

Further improvements of the modulation performance will be focused on the optimization of poling process, decreasing the polymer thickness with more efficient and thermally stable E-O polymers, and improving the FIB fabrication, which will lead to an ultra-compact device with fast modulation and low driving voltage. Such surface-normal plasmonic modulators are expandable to 2-D arrays, and can be integrated with energy-efficient optoelectronic driving circuits and low-cost continuous-wave vertical surface-emitting lasers towards the realization of out-of-plane optical interconnects.

Improving the poling efficiency can be achieved by adding a buffer layer. Therefore, modulation efficiency could be potentially improved due to the improved E-O coefficient and the sharp transition edge by improving the FIB

fabrication. Such device shows an ultra-compact device size with fast modulation and moderate driving voltage, which is promising in the application of surface-normal modulators in photonic integrated circuits together with energy-efficient optoelectronic driving circuits and low-cost continuous-wave vertical surface-emitting lasers.

Reference

[1] Q. Xu, B. Schmidt, S. Pradhan and M. Lipson, "Micrometre-scale silicon electro-optic modulator," Nature, 435, 325-327(2005).

[2] E. L. Wooten, K. M. Kissa, A.Yi-Yan, E. J. Murphy, D. A. Lafaw, P. F. Hallemeier, D. Maack, D.V. Attanasio, D. J. Fritz, G. J. McBrien and D. E. Bossi, "A review of lithium niobate modulators for fiber-optic communications systems," IEEE J. Sel. Topics Quantum Electron., 6, 69-82(2000).

[3] A. Guarino, G. Poberaj, D. Rezzonico, R. Degl'Innocenti and P. Günter, "Electro-optically tunable microring resonators in lithium niobate," Nature Photon., 1, 407-410(2007).

[4] D. W. Dolfi, M. Nazarathy and R. L. Jungerman, "40 GHz electro-optic modulator with 7.5 V drive voltage," Electron. Lett., 24, 528-529 (1988).

[5] R. W. Boyd, Nonlinear optics, second ed., Academic press, 2008.

[6] H. Huang, S. R. Nuccio, Y. Yue, J. Yang, Y. Ren, C. Wei, G. Yu, R. Dinu, D. Parekh, C.J. Chang-Hasnain and A.E. Willner. "Broadband modulation performance of 100-GHz EO polymer MZMs." J. Lightwave Technol., 30, 3647-3652 (2012).

[7] I.P. Kaminow, J.R. Carruthers, E. H. Turner and L.W. Stulz, “Thin-film $LiNbO_3$ electro-optic light modulator,” Appl. Phys. Lett., 22, 540-542(1973).

[8] Y. Q. Lu, Z. L. Wan, Q. Wang, Y. X. Xi and N. B. Ming, “Electro-optic effect of periodically poled optical superlattice LiNbO3 and its applications,” Appl. Phys. Lett., 77, 3719-3721(2000).

[9] J. Jerphagnon and S. K. Kurtz, “Optical nonlinear susceptibilities: accurate relative values for quartz, ammonium dihydrogen phosphate, and potassium dihydrogen phosphate,” Phys. Rev. B, 1, 1739(1970).

[10]V.G. Dmitriev, G. G. Gurzadyan and D. N. Nikogosyan, Handbook of nonlinear optical crystals (Springer, 2013).

[11]R. Spickermann, S. R. Sakamoto, M.G. Peters and N. Dagli, “GaAs/AlGaAs travelling wave electro-optic modulator with an electrical bandwidth> 40 GHz,” Electron. Lett., 32, 1095-1096 (1996).

[12]K. J. Weingarten, M. J. Rodwell, H. K. Heinrich, B. H. Kolner and D. M. Bloom, “Direct electro-optic sampling of GaAs integrated circuits,” Electron. Lett., 21, 765-766 (1985).

[13]L.R. Dalton, “Rational design of organic electro-optic materials,” J. Phys. Condens. Matter, 15, R897 (2003).

[14]R.S. Jacobsen, K.N. Andersen, P.I. Borel, J. Fage-Pedersen, L. H. Frandsen, O. Hansen, M. Kristensen, A.V. Lavrinenko, G. Moulin, H. Ou and C. Peucheret, “Strained silicon as a new electro-optic material,” Nature, 441, 199-202(2006).

[15]D. Chen, H. R. Fetterman, A. Chen, W. H. Steier, L. R. Dalton, W. Wang and Y. Shi, "Demonstration of 110 GHz electro-optic polymer modulators." Appl. Phys. Lett., 70, 3335-3337 (1997).

[16]S. R. Marder, B. Kippelen, A. K-Y. Jen and N. Peyghambarian. "Design and synthesis of chromophores and polymers for electro-optic and photorefractive applications," Nature 388, 845-851 (1997).

[17]L. R. Dalton, “Organic electro-optic materials,” Pure Appl. Chem., 76, 1421-1433(2004).

[18]F. Kajzar, K. S. Lee, and A. K-Y. Jen, “Polymeric materials and their orientation techniques for second-order nonlinear optics,” In Polymers for photonics applications II, Springer Berlin Heidelberg, 1-85 (2003).

[19]L. R. Dalton, B. H. Robinson, A. K-Y. Jen, W.H. Steier and R. Nielsen, “Systematic development of high bandwidth, low drive voltage organic electro-optic devices and their applications,” Opt. Mater., 21, 19-28 (2003).

[20]J. Luo, S. Huang, Z. Shi, B. M. Polishak, X.-H. Zhou and A. K-Y. Jen, "Tailored organic electro-optic materials and their hybrid systems for device applications," Chem. Mater., 23, 544-553(2010).

[21]C.Y. Lin, X. Wang, S. Chakravarty, B. S. Lee, , W. Lai, , J. Luo, A.K-Y. Jen and R. T. Chen, "Electro-optic polymer infiltrated silicon photonic crystal slot waveguide modulator with 23 dB slow light enhancement," Appl. Phys. Lett., 97, 093304 (2010).

[22]X. Wang, C.Y. Lin, S. Chakravarty, J. Luo, A.K-Y. Jen and R. T. Chen, "Effective in-device r_{33} of 735 pm/V on electro-optic polymer infiltrated silicon photonic crystal slot waveguides," Opt. Lett., 36, 882-884(2011).

[23]X. Zhang, B-S Lee, C-Y Lin, A. X. Wang and R. T. Chen, "Highly linear, broadband optical modulator based on electro-optic polymer," IEEE Photonics J., 4, 2214-2228 (2012)

[24]B-Suk Lee, C-Y Lin, A. X. Wang and R. T. Chen, "Demonstration of a linearized traveling wave Y-fed directional coupler modulator based on electro-optic polymer," J. Lightwave Technol., 29, 1931-1936 (2011).

[25]H. Ma, A. K-Y. Jen and L. R. Dalton, "Polymer-based optical waveguides: materials, process, and devices," Adv. Mater. 14 (2002) 1339-1365.

[26]A. X. Wang, B-S Lee, C-Y Lin, D. An and R. T. Chen. "Toward 120dB/Hz Spurious Free Dynamic Range: the Design and Experimental Works of Electro-Optic Polymer Linear Modulator based on Multiple-

Domain Y-fed Directional Coupler," J. Lightwave Technol., 28, 1670-1676 (2010).

[27]Y. Enami, C. T. Derose, D. Mathine, C. Loychik, C. Greenlee, R. A. Norwood, T. D. Kim, J. Luo, Y. Tian, A. K.-Y. Jen and N. Peyghambarian, "Hybrid polymer/sol–gel waveguide modulators with exceptionally large electro–optic coefficients," Nature Photon., 1, 180-185(2007).

[28]F. E. Doany, C. L. Schow, C. W. Baks, D.M. Kuchta, P. Pepeljugoski, L. Schares, R. Budd, F. Libsch, R. Dangel, F. Horst, B. J. Offrein and J. A. Kash, "160 Gb/s bidirectional polymer-waveguide board-level optical interconnects using CMOS-based transceivers," IEEE Trans. Advanced Packaging, 32, 345-359(2009).

[29]Z. Zhou, D. An, S. Tang and Ray T. Chen, "1000 V/μm pulsed poling technique for photolime-gel electro-optic polymer with room-temperature re-poling feature," Appl. Phys. Lett., 26, 3420-3422 (1998)

[30]S. Huang, J. Luo, H. L. Yip, A. Ayazi, X. H. Zhou, M. Gould, A. Chen, T. Baehr-Jones, M. Hochberg and A. K.-Y. Jen, "Efficient poling of electro-optic polymers in thin films and silicon slot waveguides by detachable pyroelectric crystals," Adv. Opt. Mater., 24, OP42-47(2012).

[31]R. Blum, M. Sprave, J. Sablotny and M. Eich, "High-electric-field poling of nonlinear optical polymers," JOSA B, 15, 318-328(1998).

[32]C. C. Teng and H. T. Man, "Simple reflection technique for measuring the electro-optic coefficient of poled polymers," Appl. Phys. Lett., 56, 1734-1736(1990).

[33]J. H. Wülbern, Jan Hendrik, Jan Hampe, Alexander Petrov, Manfred Eich, Jingdong Luo, Alex K-Y. Jen, Andrea Di Falco, Thomas F. Krauss and Jürgen Bruns, "Electro-optic modulation in slotted resonant photonic crystal heterostructures." Appl. Phys. Lett., 94, 241107(2009).

[34]S. Huang, T.D. Kim, J. Luo, S. K. Hau, Z. Shi, X.H. Zhou, H.L. Yip and A. K-Y. Jen, “Highly efficient electro-optic polymers through improved poling using a thin TiO2-modified transparent electrode,” Appl. Phys. Lett., 96, 243311(2010).

[35]R. Soref, "The Past, Present, and Future of Silicon Photonics," IEEE J. Sel. Topics Quantum Electron., 12, 1678-1687 (2006).

[36]B-S Lee, C-Y Lin, A. X. Wang, J. Luo, A-K.Y. Jen and R. T. Chen, “Bias-free electro-optic polymer based two-section Y-branch waveguide modulator with 22-DB linearity enhancement,” Opt. Lett., 34, 3277-3279 (2009).

[37]T. Baehr-Jones, M. Hochberg, G. Wang, R. Lawson, Y. Liao, P. Sullivan, L. Dalton, A. Jen and A. Scherer, "Optical modulation and detection in slotted silicon waveguides." Opt. Express, 13, 5216-5226 (2005).

[38]R. Ding, T. Baehr-Jones, Y. Liu, R. Bojko, J. Witzens, Su Huang, J. Luo, S. Benight, P. Sullivan, J-M Fedeli, M. Fournier, L. Dalton, A. Jen and M. Hochberg, "Demonstration of a low $V_{\pi}L$ modulator with GHz bandwidth based on electro-optic polymer-clad silicon slot waveguides," Opt. Express, 18, 15618-15623 (2010).

[39]D. Korn, R. Palmer, H. Yu, P. C. Schindler, L. Alloatti, M. Baier, R. Schmogrow et al. "Silicon-organic hybrid (SOH) IQ modulator using the linear electro-optic effect for transmitting 16QAM at 112 Gbit/s," Opt. Express, 21, 13219-13227 (2013).

[40]J. Leuthold, C. Koos, W. Freude, L. Alloatti, R. Palmer, D. Korn, J. Pfeifle, M. Lauermann, R. Dinu, S. Wehrli, M. Jazbinsek, P. Gunter, M. Waldow, T. Wahlbrink, J. Bolten, H. Kurz, M. Fournier, J.-M. Fedeli, Y. Hui and W. Bogaerts, "Silicon-organic hybrid electro-optical devices." IEEE J. Sel. Topics Quantum Electron., 19, 3401413(2013).

[41]A. Liu, R. Jones, L. Liao, D. Samara-Rubio, D. Rubin, O. Cohen, R. Nicolaescu and M. Paniccia, "A high-speed silicon optical modulator based on a metal-oxide-semiconductor capacitor," Nature, 427, 615-618 (2004).

[42]B. Bortnik, Y.-C. Hung, H. Tazawa, B.-J. Seo, J. Luo, A. K-Y. Jen, W. H. Steier and H. R. Fetterman, “Electrooptic Polymer Ring Resonator

Modulation up to 165 GHz," IEEE J. Sel. Topics Quantum Electron., 13, 104-110 (2007).

[43]H. Tazawa, Y.-H. Kuo, I. Dunayevskiy, J. Luo, A. K-Y. Jen, H. R. Fetterman and W. H. Steier, "Ring resonator-based electrooptic polymer traveling-wave modulator." J. Lightwave Technol., 24, 3514 (2006).

[44]G. T. Reed, G. Mashanovich, F. Y. Gardes and D. J. Thomson, "Silicon optical modulators," Nature Photon., 4, 518-526(2010).

[45]L. Liao, A. Liu, D. Rubin, J. A. B. J. Basak, Y. A. C. Y. Chetrit, H. A. N. H. Nguyen, R. A. C. R. Cohen, N. A. I. N. Izhaky and M. A. P. M. Paniccia, "40 Gbit/s silicon optical modulator for high-speed applications," Electron. Lett., 43, 1196-1197(2007).

[46]B. Bortnik, Y.-C. Hung, H. Tazawa, B.-J. Seo, J. Luo, A. K.-Y. Jen, W. H. Steier and H. R. Fetterman, "Electrooptic Polymer Ring Resonator Modulation up to 165 GHz," IEEE J. Sel. Topics Quantum Electron., 13, 104 -110(2007).

[47]W. Freude, J. Leuthold, L. Alloatti, T. Vallaitis, D. Korn, R. Palmer, C. Koos, P. Dumon, R. Baets, B. Breiten and F. Diederich, "100 Gbit/s electro-optic modulator and 56 Gbits/s wavelength converter for DQPSK data in silicon-organic hybrid (SOH) technology," IEEE Photonics Society Summer Topical Meeting Series, 96-97 (2010).

[48]L. Alloatti, R. Palmer, S. Diebold, K. P. Pahl, B. Chen, R. Dinu, M. Fournier, J.-M. Fedeli, T. Zwick, W. Freude, C. Koos and J. Leuthold, "100 GHz silicon–organic hybrid modulator," Light Sci. Appl., 3, e173(2014).

[49]A. Chen, H. Sun, A. Szep, S. Shi, D. Prather, Z. Lin, R.S. Kim and D. Abeysinghe, "Achieving higher modulation efficiency in electrooptic polymer modulator with slotted silicon waveguide," J. Lightwave Technol., 29, 3310-3318(2011).

[50]W. M. Green, M.J. Rooks, L. Sekaric, and Y.A. Vlasov, "Ultra-compact, low RF power, 10 Gb/s silicon Mach-Zehnder modulator," Opt. Express, 15, 17106-17113(2007).

[51]D. J. Thomson, F.Y. Gardes, J.M. Fedeli, S. Zlatanovic, Y. Hu, B. P. P. Kuo, E. Myslivets, N. Alic, S. Radic, G. Z. Mashanovich and G. T. Reed, "50-Gb/s silicon optical modulator," IEEE Photon. Technol. Lett., 24, 234-236(2012).

[52]X. Xiao, H. Xu, X. Li, Z. Li, T. Chu, Y. Yu and J. Yu, "High-speed, low-loss silicon Mach–Zehnder modulators with doping optimization," Opt. Express, 21, 4116-4125(2013).

[53]J.-M. Brosi, C. Koos, L. C. Andreani, M. Waldow, J. Leuthold, and W. Freude, "High-speed low-voltage electro-optic modulator with a polymer-

infiltrated silicon photonic crystal waveguide," Opt. Express, 16, 4177-4191(2008).

[54]L. Alloatti, D. Korn, R. Palmer, D. Hillerkuss, J. Li, A. Barklund, R. Dinu, J. Wieland, M. Fournier, J. Fedeli and H. Yu, "42.7 Gbit/s electro-optic modulator in silicon technology," Opt. Express, 19, 11841-11851(2011).

[55]A. Melikyan, L. Alloatti, A. Muslija, D. Hillerkuss, P. C. Schindler, J. Li, R. Palmer, D. Korn, S. Muehlbrandt, D. Van Thourhout, B. Chen, R. Dinu, M. Sommer, C. Koos, M. Kohl, W. Freudeand J. Leuthold, "High-speed plasmonic phase modulators," Nature Photon., 8, 229-233(2014).

[56]C. Haffner, W. Heni, Y. Fedoryshyn, J. Niegemann, A. Melikyan, D. L. Elder, B. Baeuerle, Y. Salamin, A. Josten, U. Koch and C. Hoessbacher, "All-plasmonic Mach-Zehnder modulator enabling optical high-speed communication at the microscale," Nature Photon., 9, 525-528(2015).

[57]A. Melikyan, K. Köhnle, M. Lauermann, R. Palmer, S. Koeber, S. Muehlbrandt, P.C. Schindler, D. L. Elder, S. Wolf, W. Heni and C. Haffner, "Plasmonic-organic hybrid (POH) modulators for OOK and BPSK signaling at 40 Gbit/s," Opt. Express, 23, 9938-9946(2015).

[58]W. Heni, C. Haffner, B. Baeuerle, Y. Fedoryshyn, A. Josten, D. Hillerkuss, J. Niegemann, A. Melikyan, M. Kohl, D.L. Elder and L. R. Dalton, "108 Gbit/s Plasmonic Mach–Zehnder Modulator with> 70-GHz Electrical Bandwidth," J. Lightwave Technol., 34, 393-400(2016).

[59] J. A. Porto, F. J. García-Vidal and J. B. Pendry, "Transmission resonances on metallic gratings with very narrow slits," Phys. Rev. Lett. 83, 2845(1999).

[60]G. D'Aguanno, N. Mattiucci, M. J. Bloemer, D. De Ceglia, M. A. Vincenti and A. Alù, "Transmission resonances in plasmonic metallic gratings," J. Opt. Soc. Am. B, 28, 253-264(2011).

[61]H.Raether, Surface polaritions on smoooth and rough surfaces and on gratings, Springer-Verlag, Berlin, 1988.

[62]S. Kim, M. J. Park, N. P. Balsara, G. Liu and A. M. Minor, "Minimization of focused ion beam damage in nanostructured polymer thin films," Ultramicroscopy, 111,191-199(2011).

[63]Y. Jouane, Y. C. Chang, D. Zhang, J. Luo, A. Jen and Y. Enami, "Unprecedented highest electro-optic coefficient of 226 pm/V for electro-optic polymer/TiO2 multilayer slot waveguide modulators," Opt. Exp., 22, 27725-27732(2014).

CHAPTER 4. MODULATION OF THIRD HARMONIC GENERATION IN POLYMERS USING METALLIC PHOTONIC CRYSTALS

In this chapter, we will discuss the modulation of third harmonic generation in polymers using metallic photonic crystals. Previous chapter has dealt with the control of transmitted light intensity by engineering the Fano resonances in metallic photonic crystals. Fast modulation was achieved by driving the devices with external RF source. Another important application of the structure is all-optical switching processing(AOSP) device for free-space interconnects. Ultra-fast communication system based on AOSP is considered to be one of potential ways to handle the rapidly increasing global communication traffic.

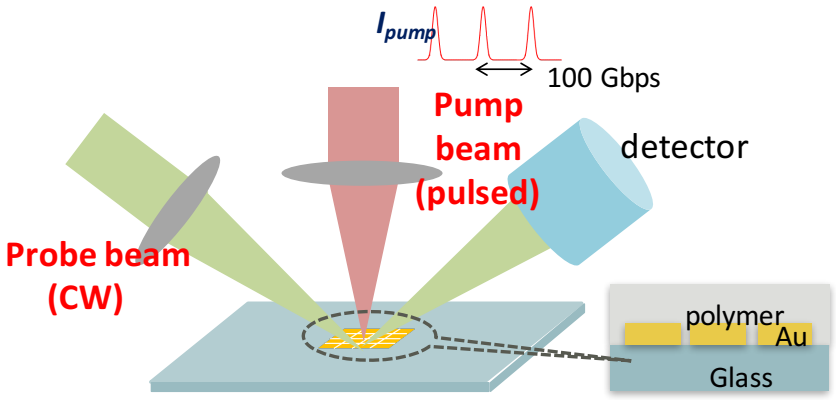

Figure 4.1: Schematic illustration of an all-optical switching processing(AOSP) device.

In all optical switching (AOS), the optical properties of a material can be modulated by the surface-normally incident pulsed beam without using external RF sources, as shown in Figure 4.1. The method of controlling the propagation of a probe light by using a pump light in Figure 4.1 is widely used for integrated photonic devices. Devices with suitable materials for AOS must exhibit large $\chi^{(3)}$ effect, as well as low linear and nonlinear optical loss. In recent years, considerable efforts have been devoted to developing photonic materials that exhibit large nonlinearity and ultrafast response at 1550 nm for AOSP devices that can be used in future optical communication systems [1-4].

An effective way to evaluate the $\chi^{(3)}$ effect for AOS application is to observe the third order harmonic generation (THG). This chapter shows our work on the approach of enhancing the effective nonlinearity through plasmonic effects, which is based on the Fano resonance generated in the organic-plasmonic hybrid nanostructure. Modulation of THG in polymers using metallic photonic crystals was observed, and over 20× enhancement factor of the THG conversion efficiency could be observed in our nanostructure.

4.1. Organic-Plasmonic Hybrid Nanostructure for AOSP

Surface-plasmon-enhanced nonlinear optical effects have been extensively investigated for nonlinear scattering, second harmonic generation (SHG), THG, two-photon absorption, four-wave mixing, AOSP and modulation [5-10]. Noble metal nanostructures have been combined with dielectric materials to generate

even stronger nonlinear effects at 1550 nm. For example, metallic nanoparticle-doped nanocomposites and hybrid dielectric-plasmonic photonic crystals have been demonstrated recently [11-12]. However, this approach has several intrinsic drawbacks such as limited tunability of resonant wavelengths, large optical loss, and relatively small volume of hot spots. Compared to nanoparticles, metallic photonic crystals can couple light into surface plasmon polariton (SPP) Bloch modes, which significantly enhance the nonlinear light-matter interaction [13-16]. Therefore, it is important to effectively combine plasmon-active photonic crystals with dielectric materials that already have large nonlinear optical susceptibility at telecom wavelengths.

Organic materials have been well studied for AOSP devices exhibiting ultra-fast third-order nonlinear optical responses, as well as low linear and nonlinear optical absorption [4, 8]. Among these organic functional materials, polymethine dyes are good candidates due to their highly delocalized π-electrons along the conjugated backbone [17-18]. Previously, an enhanced THG efficiency (3×) of a conjugated polymer on gold (Au) nanodisc/indium-tin-oxide (ITO) plasmonic photonic crystals has been demonstrated [13]. However, the enhancement is still quite low, and a relatively high threshold energy (> 2 μJ) from the pulsed laser was required for the THG emission. In addition, the 2-D nanodisc array suffers a low Q-factor, which is not suitable for practical AOSP devices.

In this chapter, we show the optical design, device fabrication, and experimental characterization of an organic-plasmonic hybrid nanostructure based

on high-Q Au nanopatch arrays infiltrated with a polymethine-based polymer to enhance the intensity of third-order harmonic generation. Numerical simulations based on finite-element analysis demonstrated localized SPPs from the two-dimensional (2-D) Au nano-patch arrays inside the polymer layer. Quantitative measurements of the THG intensity indicate that the hybrid nanostructure platform provides 20 × higher THG emissions, which is significantly greater than that of the previously work [13]. In addition, the threshold of the energy from the incident pulsed laser is as low as 15 pJ.

4.2. Theoretical Study

The device structure is schematically shown in Figure 4.2, which consists of 2-D arrays of Au patches on top of a glass substrate coated by a polymer thin film. In these hybrid organic-plasmonic devices, polymer (AJBC 1725) based on an anionic polymethine salt was used as the nonlinear medium to provide the THG effect. By careful structural optimization, AJBC 1725 shows excellent compatibility with the amorphous polycarbonate host polymer to form high optical quality composite films, which shows very large third order nonlinear susceptibility, low optical loss, and excellent optical power handling capability [17].

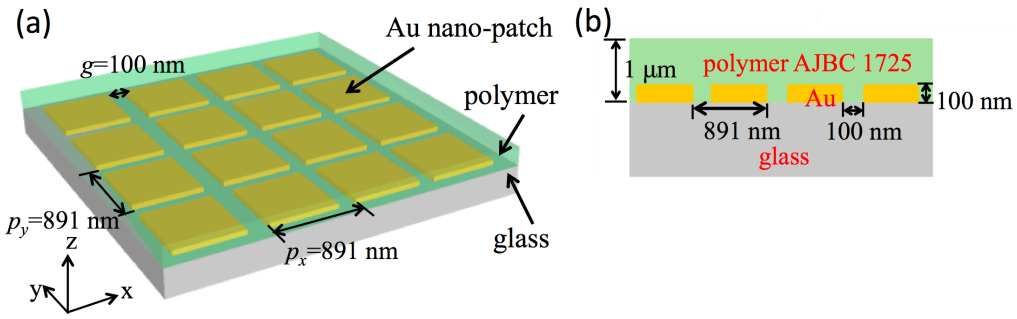

Figure 4.2: (a) Sketch of the 2-D gold nano-patch arrays on a glass substrate. The top layer is the nonlinear optical polycarbonate composite films doped with 50 wt% AJBC 1725(not to scale); (b) the cross-sectional view of the device structure.

We chose 2-D nano-patch arrays as the plasmonic resonator due to the symmetry of the structure. The device is insensitive to the angle of polarization within the plane parallel to the Au patch surface, which is favorable as a resonator over 1-D nanowire arrays that are polarization-dependent [19, 20]. The geometric dimensions are shown in Figure 4.2(a), where the periodicities p_x=p_y=891 nm, and the gap size between any two adjacent patches g=100 nm. The thickness of the Au and polymer is designed at 100 nm and 1 μm respectively, as shown in Figure 4.2(b).

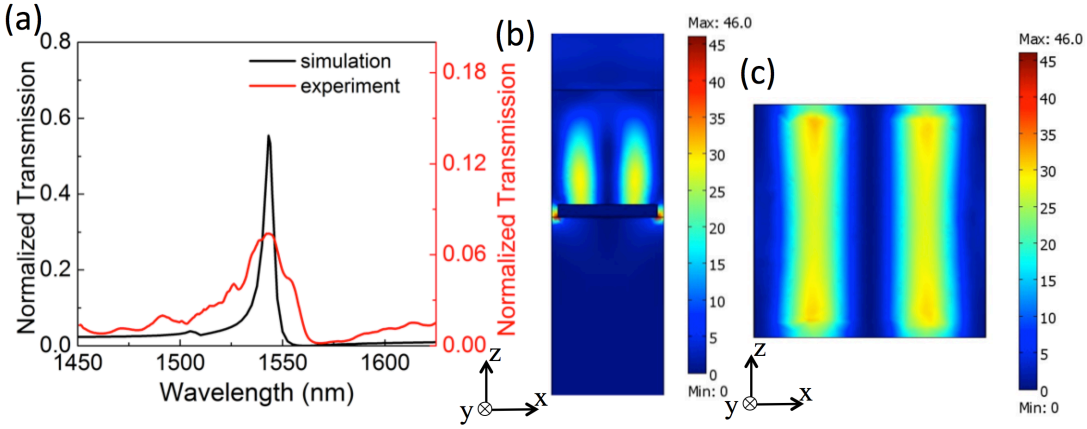

Figure 4.3: The simulated (black) and experimental (red) transmission spectra are shown in (a). The intensity distribution of 2-D periodic gold arrays for normally incident x-polarized E-field (b) from the cross-sectional view (c) from the top view (100 nm from the Au surface).

The electrical field enhancement and the optical transmission were theoretically investigated by conducting a three-dimensional (3-D) finite element simulation using the RF module within Comsol 3.5a. A plane wave was used as the excitation light with electric field polarized along the x-axis and a periodic boundary condition was applied in the simulation. Under normal incident, the excitation of SPPs is described by the zero-order relation [21]

$$\lambda_{min} = p_x \left(\sqrt{\frac{\varepsilon_{Au}\varepsilon_d}{\varepsilon_{Au}+\varepsilon_d}} \right) \tag{4.1}$$

$$p_x = p_y \tag{4.2}$$

The wavelength (λ_0) of the SPP is determined by the permittivities of the polymer (ε_d) and Au (ε_{Au}), and the periodicity of the 2-D patches (p). The refractive index of the polymer AJBC 1725 was measured to be 1.8 by ellipsometry. At the near infrared wavelengths between 1400 nm and 1800 nm, a strongly asymmetric Fano resonance centered at 1543 nm was observed from the simulated wavelength range, as shown in Figure 4.3(a). The discrete guided modes induced by the Bragg-grating-modulated SPPs couple to the broadband resonance in the narrow slits, resulting in strongly asymmetric resonances with a sharp bandgap [22, 23]. A minimum transmission state at 1558 nm is shown in the transmission spectrum, which is a clear indication of the formation of the plasmonic bandgap. From the transmission spectrum, the Q-factor was determined to be as high as 257.

Figure 4.3(b) and 4.3(c) show the intensity distribution $|E/E_0|^2$ (where E_0 is the peak electric field of the incident light) associated with the SPPs at the Au-polymer interface of 1543 nm from the cross sectional view and the top view, respectively. Enhanced electric fields are located over the surface of the gold array, and the maximum enhancement factor of intensity $|E/E_0|^2$ is as high as 46. In a typical nanoplasmonic system, the field localization of a nanoantenna usually concentrates in a “hot spot” with the volume of a few cubic nanometers in the gap region [24], which limits the overall enhancement. However, the concentrated electric field in the 2-D Au nanopatch array covers almost the entire Au patch

surface and extends deeply into the polymer layer, resulting in a relatively uniform electric field enhancement over a large volume.

4.3. Experimental Characterization

Polymethine dye AJBC1725 was prepared in our previous work [18]. The polymethine dyes were mixed with APC (50% w/w) to prepare a guest-host polymer composite, then dissolved in dibromomethane with a concentration of ~5 wt%. Figure 4.4(a) shows the photograph of a spin-coated polymer thin film on a glass cover slide and has a thickness of ~1 μm. We started the fabrication of the plasmonic structure by depositing a 100 nm Au thin film on a glass substrate (index is 1.5023) by thermal evaporation with a deposition rate of 8 Å/Sec. The 2-D Au nano-patch arrays were patterned by focused-ion beams (FIB), with a gallium ion current of 14.5 pA and a dose of 5 mC/cm^2. A scanning electron microscopy (SEM) image of the 2-D nano-patch arrays after the FIB milling is shown in Figure 4.4(b), which indicates that highly ordered 2-D arrays of nano-patches were formed with slightly rounded corners (curvature less than 15 nm). A thin film (1 μm) of nonlinear polymer composite was spin-coated on top of the Au layer to form the hybrid plasmonic-organic structure at 1900 rpm for 120 s. The optical image of the fabricated plasmonic-organic device is shown in Figure 4.4(c). In order to compare the THG efficiency, a control device was also fabricated, with 1 μm polymer on top of a 100 nm Au thin film without any plasmonic structure pattern.

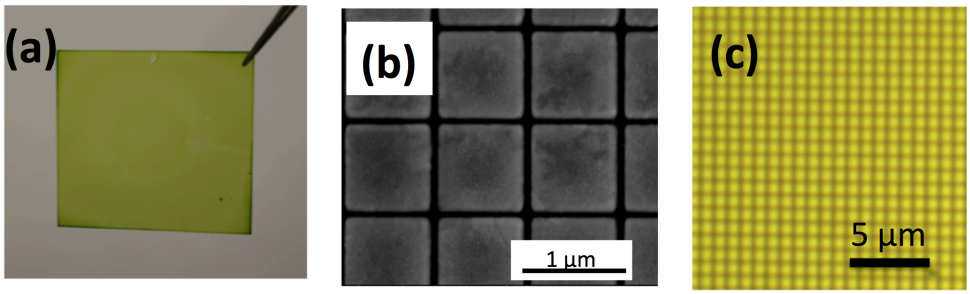

Figure 4.4: (a) A representative photograph of the nonlinear polymer thin film on a glass substrate; (b) The SEM image of the plasmonic structure after FIB process, showing highly ordered nano-patch arrays; (c) The optical image of the plasmonic structure.

The experiment setup of the optical transmission measurement has been discussed in the previous work [25]. From the transmission spectrum in Figure 4.5(a), an asymmetric Fano resonance peak is shown on the measured wavelength range, with the resonant peak centered at 1543 nm and a full width half maximum of 22 nm. Therefore, the measurement showed a Q-factor of 70.1, which is less the results of the simulation mentioned previously. The enlarged bandgap of the Fano resonance and the reduced Q-factor are possibly due to the non-ideal Au film quality, fabrication defects, and the imperfect beam collimation.

The experimental setup for observing THG signals from the plasmonic-organic device is shown in Figure 4.5(a). A fiber-based femtosecond laser (Calmar Laser, FPL-03CFF) was launched to pump the polymer-Au hybrid

plasmonic device with a repetition frequency of 20 MHz. The output light was collimated by a 40× objective lens (NA=0.65). A dichroic mirror was used to reflect the pump laser centered at 1550 nm, while also allowing the transmission of the THG wavelengths centered at 517 nm. The reflected beam was focused by a 100× objective lens (NA=0.90). The plasmonic-organic sample was mounted at the focal plane of the objective lens on a three-dimensional translation stage. After focusing, the diameter of the spot size of the pump laser was ~ 8 μm. The THG emission was imaged by a colored CCD camera (Thorlabs, DCC1645C) in the far field after filtering the pump laser using a bandpass filter (Thorlabs, FB520-10). The captured high-resolution images from the CCD in Figure 4.5(b) and Figure 4.5(c) compare qualitatively the THG emission from the polymer with the plasmonic structures and from the polymer without the plasmonic structure (a pure gold thin film, control device). The qualitative comparison indicates that the polymer with plasmonic structure has a much greater THG efficiency ($\eta = I_{THG}/I_{pump}$) at frequency $\omega_{THG} = 3\omega_0$, which is due to the electric field enhancement of the surface plasmon resonance at the organic-plasmonic structure.

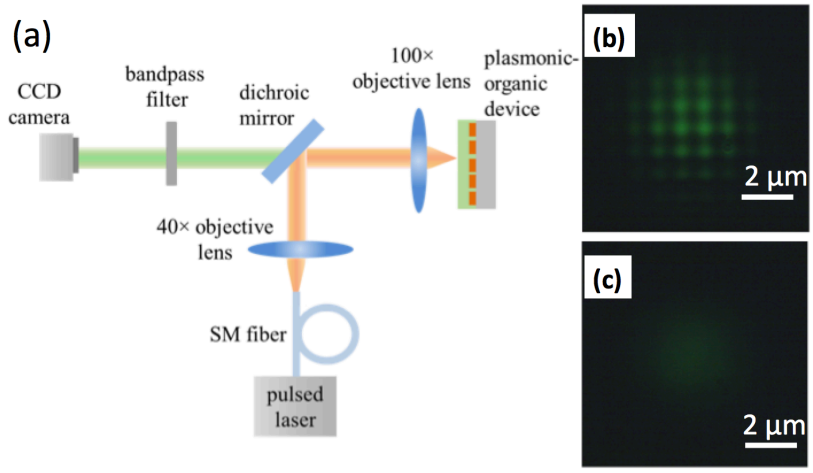

Figure 4.5: (a) The experimental setup of the THG signal imaging system for the devices; (b) The captured THG signal intensities from the plasmonic-organic structure; (c) The captured THG intensities from polymer without the plasmonic structure.

Further study was focused on the quantitative measurement of the intensities of THG signals from the hybrid organic-plasmonic device. The CCD camera was replaced by a photomultiplier tube, which was used to measure the intensity of the THG signals. A fiber-based tunable filter was used to manually select the wavelength of the pumping light with a narrow spectral bandwidth of 3.2 nm, tuning the output wavelength from 1532 nm to 1565 nm. Figure 4.6(a) shows the THG response by tuning the wavelengths of the fs-laser. The measured results show that the hybrid organic-plasmonic structure provides as high as 21.6× the enhancement of the response compared to that of the control device. The peak of the enhancement factor in the inset figure in Figure 4.6(a) matches the resonant

peak of the measured spectrum, which confirms the enhancement from the localized SPPs at the Au-polymer interface.

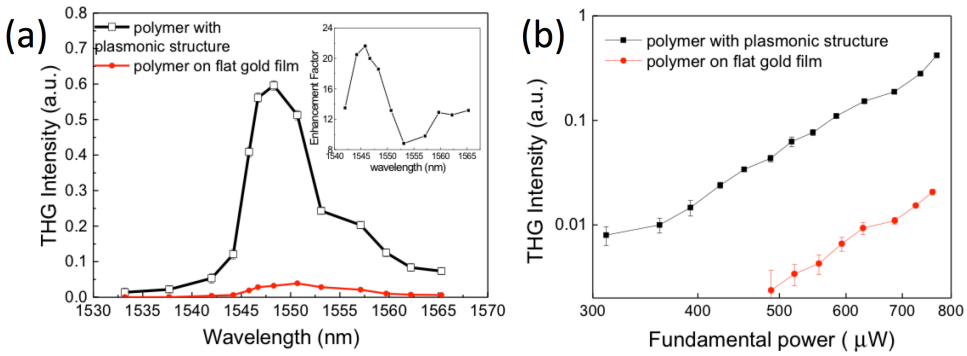

Figure 4.6: (a) The THG wavelength dependence of the nonlinear optical polymer composite with and without plasmonic structure respectively. The inset figure shows the enhancement factors as a function of wavelengths. (b) The THG power dependence of the polymer with (black) and without plasmonic structure (red), respectively.

The dependence of the THG intensity with respect to the pumping power at 1550 nm was also investigated in this work. A fiber-based attenuator was connected with the output of the femtosecond laser in order to adjust the intensity of the pumping light coupled into the system. The THG (electric field intensity $I_{3\omega}$, frequency 3ω) from a fundamental light (electric field intensity I_{ω}, frequency ω) is expected to have a cubic dependence on the fundamental power in the measurement for perfect phase matching and maximum mode overlap between

the fundamental mode and the third harmonic wavevectors [26, 27]. The power dependence of THG is plotted in Figure 4.6(b). The THG was much stronger in the polymer with plasmonic structures compared with that of the control device within the measured power range. Due to the presence of the SPPs at the polymer/Au interfaces, the average enhancement factor reaches as high as 20×. THG was observed through the entire measurement range from 312 μW to 773 μW in the hybrid plasminic-organic structure. With a repetition rate at 20 MHz, the pulsed energy for the THG emission threshold is as low as 15 pJ, which is reduced by a factor of over 10^5 compared to the previously reported results [13]. For the control device, the THG emission could only be observed above the threshold of the fundamental power of 485 μW. Therefore, it can be concluded from the power-dependence measurement that the THG from the organic-plasmonic hybrid structure is considerably higher than that from a pure polymer thin film.

4.4. Summary

In conclusion, we have designed and fabricated a hybrid plasmonic-organic nanostructure to enhance the THG efficiency at the telecom wavelengths of 1550 nm. Numerical simulations show that the 2-D plasmonic structure creates a large-volume optical field enhancement throughout the bulk polymer, which is proved by the qualitative comparison of the THG intensity from the images of a CCD camera. Further experiments show that over 20× enhancement factor of the THG conversion efficiency could be observed in our nanostructure due to the electric

field localization at the SPP resonant wavelengths. This hybrid plasmonic-organic nanostructure opens a new route for future AOSP devices.

Reference

[1] M. Amin, M. Farhat and H. Bağcı, "A nonlinear plasmonic resonator for three-state all-optical switching," Opt. Express 22, 6966-6975(2014).

[2] A. Martínez, J. Blasco, P. Sanchis, J. Galán, J. García-Rupérez, E. Jordana, P. Gautier, Y. Lebour, S. Hernández, R. Spano, R. Guider, N. Daldosso, B. Garrido, J. M. Fedeli, L. Pavesi and J. Martí, "Ultrafast all-optical switching in a silicon-nanocrystal-based silicon slot waveguide at telecom wavelengths," Nano Lett., 10, 1506-1511(2010).

[3] V. R. Almeida, C. A. Barrios, R. R. Panepucci and M. Lipson,"All-optical control of light on a silicon chip," Nature, 431, 1081-1084(2004).

[4] C. Koos, P. Vorreau, T. Vallaitis, P. Dumon, W. Bogaerts, R. Baets, B. Esembeson, I. Biaggio, T. Michinobu, F. Diederich, W. Freude and J. Leuthold, "All-optical high-speed signal processing with silicon–organic hybrid slot waveguides," Nat. Photonics, 3, 216-219 (2009).

[5] M. Hochberg, T. Baehr-Jones, G. Wang, M. Shearn, K. Harvard, J. Luo, B. Chen, Z. Shi, R. Lawson, P. Sullivan, A. K. Y. Jen, L. Dalton and A. Scherer, "Terahertz all-optical modulation in a silicon-polymer hybrid system," Nat. Mater., 5, 703-709(2006).

[6] J. I. Dadap, J. Shan, K. B. Eisenthal and T. F. Heinz, "Second-harmonic Rayleigh scattering from a sphere of centrosymmetric material," Phys. Rev. Lett., 83, 4045(1999).

[7] M. Kauranen and A. V. Zayats, "Nonlinear plasmonics," Nat. Photonics, 6, 737-748(2012).

[8] W. Cai, A. P. Vasudev and M. L. Brongersma, "Electrically controlled nonlinear generation of light with plasmonics," Science, 333, 1720-1723(2011).

[9] W. Wenseleers, F. Stellacci, T. Meyer-Friedrichsen, T. Mangel, C. A. Bauer, S. JK Pond, S. R. Marder and J. W. Perry, "Five orders-of-magnitude enhancement of two-photon absorption for dyes on silver nanoparticle fractal clusters," J. Phys. Chem. B, 106, 6853-6863(2002).

[10]S. Palomba, M. Danckwerts and L. Novotny, "Nonlinear plasmonics with gold nanoparticle antennas," J. Opt. A: Pure Appl. Opt., 11, 114030(2009).

[11]M. Abb, P. Albella, J. Aizpurua and O. L. Muskens. "All-optical control of a single plasmonic nanoantenna-ITO hybrid," Nano Lett., 11, 2457-2463(2011).

[12]C. Lu, X. Hu, Y. Zhang, Z. Li, H. Yang and Q. Gong, "Large Nonlinearity enhancement of Ag/MEH-PPV nanocomposite by surface plasmon resonance at 1,550 nm," Plasmonics, 7, 159-165(2012).

[13]H. B. Liao, R. F. Xiao, H. Wang, K. S. Wong and G. K. L. Wong, “Large third-order optical nonlinearity in Au: TiO_2 composite films measured on a femtosecond time scale,” Appl. Phys. Lett., 72, 1817(1998).

[14]S. Chen, W. Wong, Y. Pun, K. Cheah and G. Li, “Surface plasmon-enhanced third harmonic generation from gold–polymer hybrid plasmonic crystal,” Adv. Opt. Mater., 1, 522-526(2013).

[15]D. J. Ironside and J-T Shen, “Orders of magnitude enhancement of optical nonlinearity in subwavelength metal-nonlinear dielectric gratings,” Appl. Phys. Lett., 102, 021907(2013).

[16]G. A. Wurtz, and A. V. Zayats, “Nonlinear surface plasmon polaritonic crystals,” Laser & Photon. Rev., 2, 125-135(2008).

[17]X. Yang, A. Ishikawa, X. Yin and X. Zhang, "Hybrid photonic- plasmonic crystal nanocavities," ACS Nano, 5, 2831-2838(2011).

[18]A. Scarpaci, A. Nantalaksakul, J. M. Hales, J. D. Matichak, S. Barlow, M. Rumi, J.W. Perry and S. R. Marder, “Effects of dendronization on the linear and third-order nonlinear optical properties of bis (thiopyrylium) polymethine dyes in solution and the solid state,” Chem. Mater., 24, 1606-1618(2012).

[19]Z. Li, Y. Liu, H. Kim, J. M. Hales, S. H. Jang, J. Luo, T. Baehr-Jones, M. Hochberg, S. R. Marder, J. W. Perry and A. K.-Y. Jen, “High-optical-quality blends of anionic polymethine salts and polycarbonate with

enhanced third-order non-linearities for silicon-organic hybrid devices," Adv. Mater., 24, OP326-OP330(2012).

[20]M. Grande, M. A.Vincenti, T. Stomeo, G. Morea, R. Marani, V. Marrocco, V. Petruzzelli, A. D'Orazio, R. Cingolani, M. De Vittorio, D. de Ceglia and M. Scalora, "Experimental demonstration of a novel bio-sensing platform via plasmonic band gap formation in gold nano-patch arrays," Opt. Express, 19, 21385-21395(2011).

[21]B. D. Lucas., J.-S. Kim, C. Chin and L. Jay Guo, "Nanoimprint lithography based approach for the fabrication of large-area, uniformly oriented plasmonic arrays," Adv. Mater., 20, 1129-1134(2008).

[22] H. Raether, Surface Polaritons on Smooth and Rough Surfaces and on Gratings, Springer-Verlag, Berlin (1988).

[23]A. Christ, T. Zentgraf, J. Kuhl, S. G. Tikhodeev, N. A. Gippius and H. Giessen, "Optical properties of planar metallic photonic crystal structures: experiment and theory," Phys. Rev. B, 70, 125113(2004).

[24]B. Luk'yanchuk, N. I. Zheludev, S. A. Maier, N. J. Halas, P. Nordlander, H. Giessen and C. T. Chong, "the Fano resonance in plasmonic nanostructures and metamaterials," Nature Mater., 9, 707-715 (2010)

[25]R. M. Bakker, A. Boltasseva, Z. Liu, R. H. Pedersen, S. Gresillon, A. V. Kildishev, V. P. Drachev and V. M. Shalaev, "Near-field excitation of nanoantenna resonance," Opt. Express, 15, 13682-13688(2007).

[26]F. Ren, X. Wang and A. Wang, “Thermo-optic modulation of plasmonic bandgap on metallic photonic crystal slab,” Appl. Phys. Lett., 102, 181101 (2013).

[27]R. Boyd, Nonlinear Optics, Ch. 2, Academic Press (1992).

[28]B. Corcoran, C. Monat, C. Grillet, D. J. Moss, B. J. Eggleton, T. P. White, L. O'Faolain and T. F. Krauss, “Green light emission in silicon through slow-light enhanced third-harmonic generation in photonic-crystal waveguides,” Nat. Photonics, 4, 206-210(2009).

CHAPTER 5. EFFECT OF FINITE METALLIC PHOTONIC CRYSTAL SIZE ON RAYLEIGH ANOMALY-SURFACE PLASMON POLARITON RESONANCES

Fano resonance in metallic photonic crystal due to the coupling between Rayleigh anomaly (RA) and surface plasmon polariton (SPP) resonances has been briefly discussed in Chapter 1. Chapter 2, 3 and 4 have discussed the electro-optical modulation and third harmonic generation modulation of Fano resonances for free-space interconnects. Driven by chip-scale optical interconnects, it is becoming attractive to minimize the footprint of metallic photonic crystals. When minimizing the size of the metallic photonic crystals, assuming an infinite device size becomes invalid in modeling and analysis of Fano Resonance. However accurate modeling of the structure using finite difference time domain (FDTD) or finite element method (FEM) requires large computer memory and takes several hours. In this chapter, we present a simple method to investigate the effect of finite grating size on RA and SPP resonances of plasmonic gratings based on the combination of rigorous coupled-wave analysis (RCWA) and finite aperture diffraction. Our method effectively shows that the bandgap edges of RA-SPP resonances are broadened as the grating size shrinks due to the angular dependence of RA-SPP resonances, which agrees very well with experimental results quantitatively. The simulation time and memory resources using our method can be greatly reduced compared to FDTD and FEM.

5.1. Rayleigh Anomaly-Surface Plasmon Polariton Resonances

Extraordinary optical transmission (EOT) resulted from RA-SPP resonances through periodic subwavelength diameter airholes or narrow slits in metal film has been the subject of intensive research in plasmonics for many years [1-4]. From the discussion in previous chapters, it can be seen that the mechanisms underlying the EOT in these grating or photonic crystal systems can be attributed to the complex interaction among SPPs, RAs, waveguide modes, and the Fabry-Perot resonances inside the airholes or slits [5-9]. Rayleigh anomaly resonances in periodic structures are associated with both plasmonic and dielectric gratings. For the simplest structure consisting of a thin metallic grating on top of a glass substrate as shown in Figure 1.9 in chapter 1, waveguide modes and F-P resonances inside the slits are not supported, therefore, the EOT phenomenon is described by the coupling of RAs on one side of the film with SPP Bloch waves (SPP-BWs) on the opposite side. Nevertheless, such theoretical analysis was based on infinitely large metallic grating size and experimental characterization used very large gratings (millimeter size), which can be a good approximation to the modeling. Assuming an infinite size metallic grating in modeling is invalid and implementing a large size device is not practical for these new applications. However, to take this ‘finiteness’ into account is quite troublesome. Finite element analysis calculations can be useful but if the grating size is quite large (but finite), large computer resources and long calculation time are required. There are a few semi-analytic methods that basically treat the finite grating as an

array of electromagnetic radiators or scatters [15-16]. Nevertheless, they are too complicated and are not adequate for large gratings either.

In the past years, guided-mode resonance filters (GMRFs) using dielectric gratings with finite grating periods and finite input beam size have been analyzed using different numerical approaches [17-19]. In this chapter, we present the theoretical study of the effect of finite size on RA-SPP resonances in metallic gratings that are not presented in dielectric GMRFs. The analysis is based on the combination of the finite aperture diffraction and the transmission spectrum of the infinite metallic grating obtained by the RCWA method [20]. In an effort to verify the theoretical analysis, experimental data of the transmission properties of the gold(Au)/glass grating are presented and compared with the simulation results. The comparison clearly confirmed that the broadening in RA-SPP resonances matched very well with the modeling as the size of the grating shrinks.

5.2. Theoretical Study

For a structure like Figure 2.1 in chapter 2, the coupling between RAs and SPPs on metal/dielectric interfaces leads to EOT with narrow spectral features at specific wavelengths [21-23]. Such resonances have been demonstrated to show sensitivity to angular variations. Figure 5.1 shows the simulation results of the total transmitted optical power using RCWA from 600 nm to 1900 nm by scanning the incident angle α from 0 to 3.2˚, with a simulation step of 0.016˚. In the wavelength range of 1000 nm to 1900 nm, two Fano Resonances are formed

due to the first order RA-SPPs for surface-normally incident TM light: one at the top air-Au interface at 1634 nm, and the other at the bottom Au-glass interface at 1076 nm. Higher order RA-SPPs can also be observed, and a minimum transmission of second order RA-SPPs at the Au-glass interface is shown at 823 nm. With an incident angle of the incoming light, symmetry is broken and each pair of RA-SPPs splits into a high and low-energy branch. The wavelength separation between the two branches increases with the incident angle α, as shown in Figure 5.1.

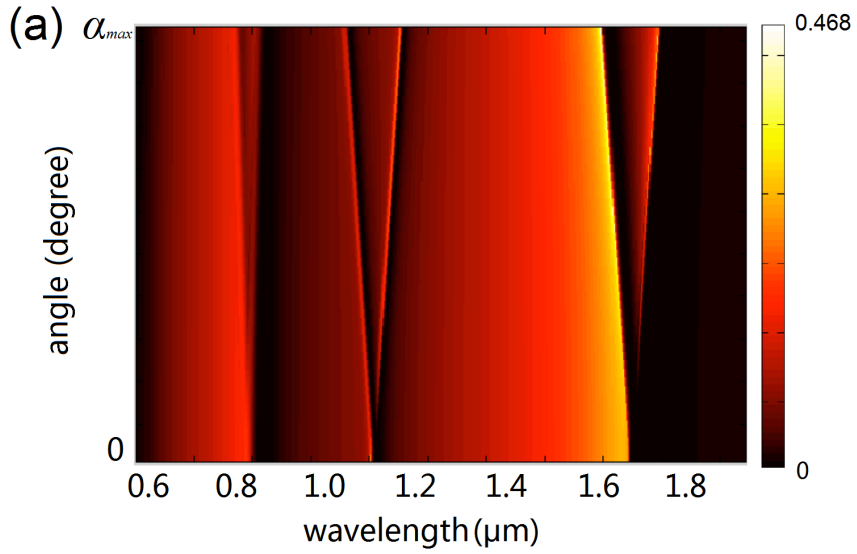

Figure 5.1: RCWA simulation of total transmitted power with different angular incidences.

In the next step, we will consider the effect of finite size of the grating. As 100nm Au film is almost completely opaque to visible and near-infrared

wavelength, we can treat the structure as an infinite grating with an aperture window of D, where D is the size of the grating as shown in Figure 1.9 in Chapter 1. When a plane wave $U(x)$ passes through a finite grating, the electric field is modulated by both effects of the infinite plasmonic grating and the aperture window. Therefore, the near-field electric field amplitude can be expressed as

$$E(x) = g_{gr}(x) f_{ap}(x) U(x), \tag{5.1}$$

where $g_{gr}(x)$ denotes the transfer function due to the infinite grating, and $f_{ap}(x)$ is the aperture window function. Based on Fraunhofer diffraction theory [24], the electric field measured at the far field becomes the spatial Fourier transform of the near-field distribution, which is

$$E(\theta) \propto F\left[g_{gr}(x) f_{ap}(x) U(x) \right]\Big|_{f_x = \frac{x}{\lambda z} = \frac{\theta}{\lambda}}, \tag{5.2}$$

where θ is the angular divergence of the diffracted light. Since $F[U(x)] \sim \delta(f_x - \alpha/\lambda)$, Equation 5.2 becomes

$$\begin{aligned} E(\theta) &\propto F\left[g_{gr}(x) f_{ap}(x) \right]\Big|_{f_x = \frac{\theta - \alpha}{\lambda}} \\ &= \int G_{gr}\left(\frac{\theta - \alpha}{\lambda} - \xi \right) F_{ap}(\xi) d\xi, \end{aligned} \tag{5.3}$$

where $G_{gr}(f_x)$ and $F_{ap}(f_x)$ denote the spatial Fourier transforms of $g_{gr}(x)$ and $f_{ap}(x)$, respectively, and F_{ap} is a well-known sinc function. With that, we can solve the transmitted intensity $I(\theta)$ at the far field by calculating the convolution given by

$$I(\theta) \propto \left| \int G_{gr}\left(\frac{\theta - \alpha}{\lambda} - \xi \right) \mathrm{sinc}(D\xi) d\xi \right|^2. \tag{5.4}$$

Considering that, for subwavelength grating, only zeroth-order diffraction mode exists in the long wavelength range and its diffraction angle is equal to the incident angle, we can write $G_{gr}(\theta/\lambda-\alpha/\lambda) \sim G_0(\alpha)\delta(\theta/\lambda-\alpha/\lambda)$, where $|G_0(\alpha)|^2$ represents the transmitted optical power when the incidence angle is α. Therefore. Equation 5.4 can be further approximated as

$$I(\theta) \propto \left|G_0(\alpha)\right|^2 \operatorname{sinc}^2\left[D\left(\frac{\theta-\alpha}{\lambda}\right)\right]. \tag{5.5}$$

Using this combined analytical-numerical approach, the overall transmission spectra of the finite plasmonic grating are plotted in Figure 5.2 (a)~(c). The broadening of RA-SPP resonances due to the reduction of the grating size can be clearly seen from the simulation results, especially for the fundamental resonances in Figure 5.2 (b) and (c).

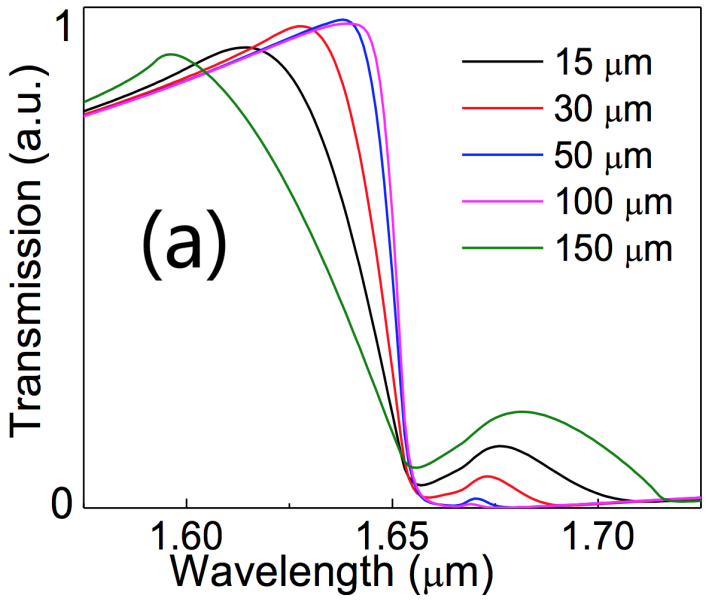

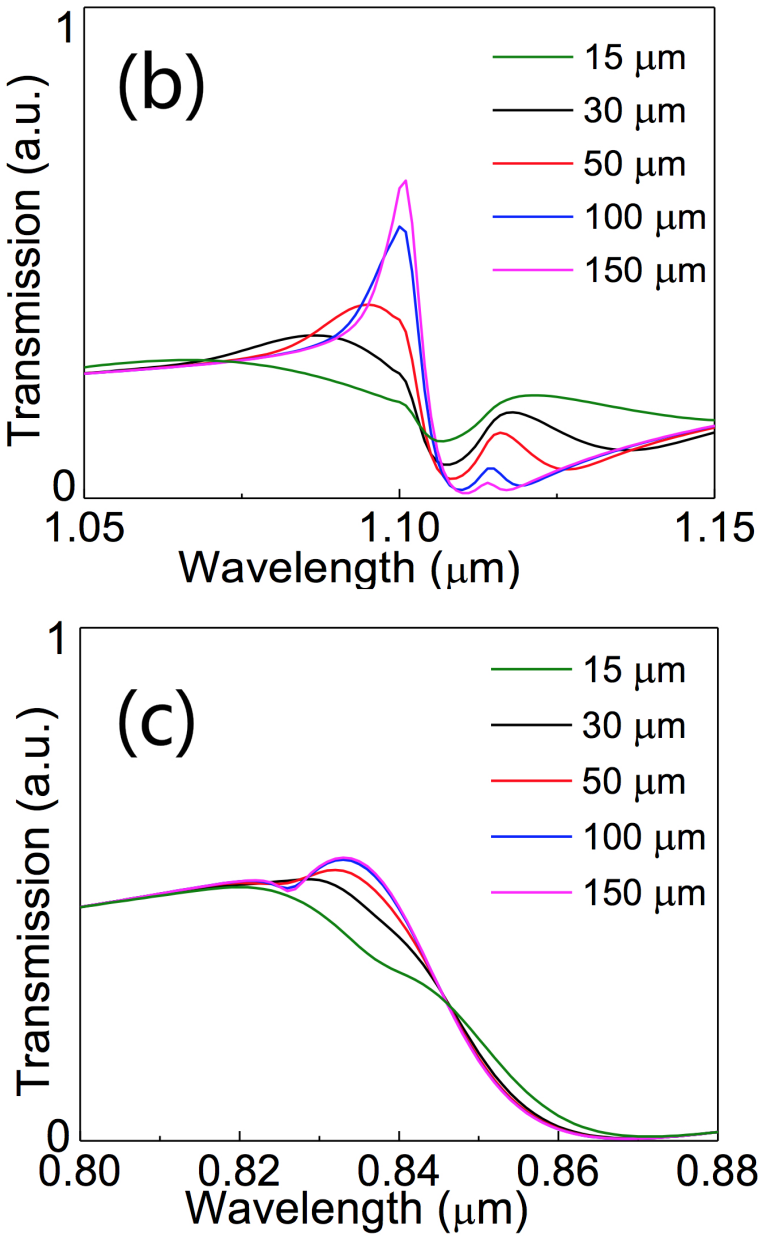

Figure 5.2: (a) Summary of the simulated results are of (a) first order RA-SPP at Au/glass interface (b) first order RA-SPP at Au/air interface (c) second order RA-SPP at Au/glass interface.

5.3. Experimental Characterization

To verify our calculation, we fabricated an array of subwavelength Au gratings on a glass substrate. Au thin film was deposited onto the glass substrate by thermal evaporation with a deposition rate of 5 Å/sec, resulting in a film thickness of 100 nm. An array of Au gratings was fabricated by focused-ion beams (FIB) with grating sizes of 15 μm, 30 μm, 50 μm, 100 μm, and 150 μm. The nanoscale structures were patterned by gallium ion beams with ion energy and current controlled at 30 kV and 30 pA, respectively. Figure 5.3(a) shows the SEM image of the fabricated plasmonic grating. Controlling the width of the gap and minimizing the fabrication defects are crucial for obtaining sharp RA-SPP resonances for the device. During the fabrication process, the geometrical dimensions are precisely controlled and smooth Au slits were obtained using FIB. Figure 5.3(b) shows the experimental setup of measuring the transmission spectrum. A broadband supercontinuum white light source (NKT Photonics) with free-space collimated beam was used as input source. A polarizer was used to generate a linearly TM polarized light with electric field polarized perpendicular to the slit direction. The beam size was reduced to ~500 μm by using a free-space convex and a concave lenses. Compared with the size of the plasmonic gratings, the beam spot size is much larger. Therefore, the incident light can be approximated as a plane wave. The device was mounted on a five axis stage, which allowed precise adjustment of the linear translations as well as the incident

angle within 0.0029˚. The output light was then focused through a 40× objective lens (NA=0.65) and coupled into an optical spectrum analyzer (HP70951A).

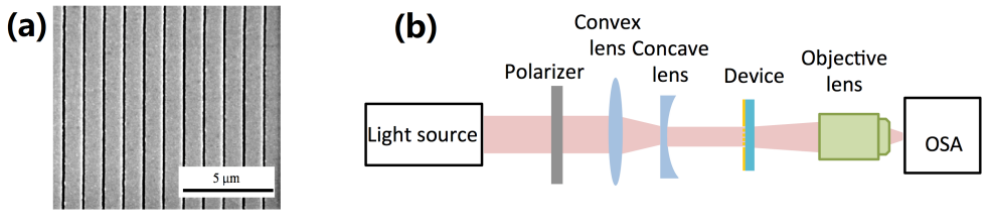

Figure 5.3: (a) SEM image shows the fabricated grating with smooth slits; (b) Transmission measurement setup.

The normalized optical transmission spectra were measured for the gratings size of 15 μm, 30 μm, 50 μm, 100 μm, and 150 μm. Figure 5.4 (a)~(c) shows the zoomed-in transmission at the wavelength range of 1250-1700nm, 1000-1250nm, and 750-1000nm, respectively. As predicted by the model and Figure 5.2 (a)~(c), when the size of the grating shrinks, the RA-SPP resonances became less pronounced. The RA-SPP resonances with the sharpest transition edge always occur on the 150 μm plasmonic grating. In order to quantitatively compare our model with experimental results, we summarized the transition edge of the RA-SPP resonances in Figure 5.4(d) representing the first-order RA-SPPs at Au/glass (~1634 nm) and Au/air interfaces (~1076 nm), and the second order RA-SPPs at the Au/glass (~823 nm) interface. The bandwidth of the transition edge is accounted as the wavelength range from the maximum transmission (RA) to the minimum transmission (SPP-BW). For the first-order RA-SPPs at Au/glass and

Au/air interfaces, the modeling results of the bandwidth of the transition edge matched very well with the experimental results. However, when we compare the shape of the transmission spectra, the small peaks of the transition edge in the simulation results due to the low-energy branch were not observed in the experimental results. This is possibly due to the fluctuation of the light source or the measurement error at low optical power as the grating size shrinks. The measured transition edges of the higher order RA-SPPs within 750-1000nm are broader than the modeling results. In addition, thermally evaporated Au film shows higher imaginary part of the dielectric permittivity than bulk Au adopted in the simulation, which results in the higher loss at shorter wavelength range since the electro-magnetic waves penetrate deeper into the metal.

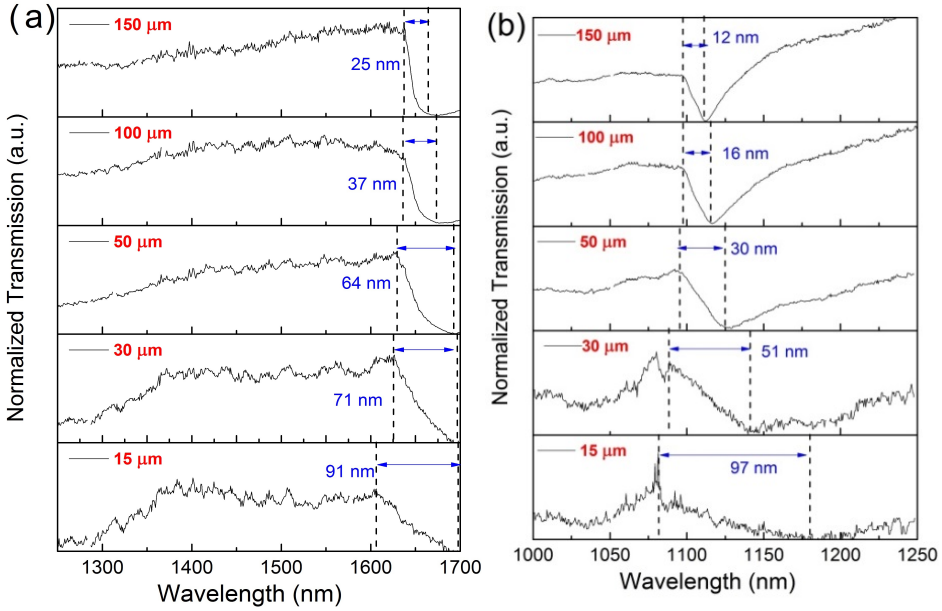

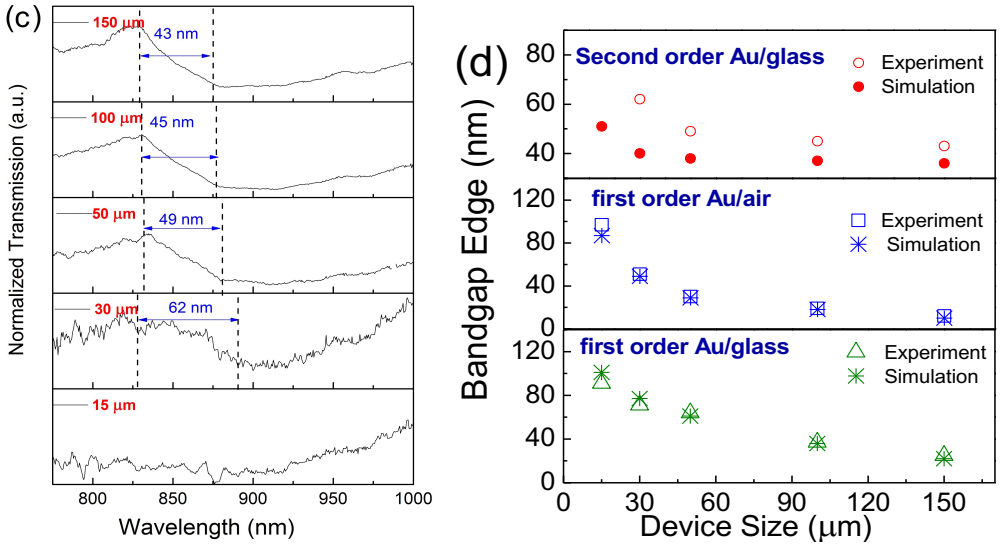

Figure 5.4: Measured spectra showing the transmission within (a) first order Au/glass within 1250-1700 nm (b) first order Au/air within 1000-1250 nm and (c) second order Au/glass within 750-1000 nm; (d) Summary of the simulated and experiment results of transitional edges vs. device size.

5.4. Summary

In this chapter, we presented a simple method to investigate the effect of finite grating size on RA-SPP resonances of plasmonic gratings based on the combination of RCWA and finite aperture diffraction. As predicted by this model, the transition edges of RA-SPP resonances are broadened as the grating size shrinks due to the angular dependence of RA-SPP resonances. The experimental results agree well with simulated results quantitatively. This study points out the theoretical limit of miniaturizing subwavelength plasmonic gratings for optical sensing and optical modulation.

Reference

[1] Martínez, J. Blasco, P. Sanchis, J. Galán, J. García-Rupérez, E. Jordana, P. Gautier, Y. Lebour, S. Hernández, R. Spano, R. Guider, N. Daldosso, B. Garrido, J. M. Fedeli, L. Pavesi and J. Martí, "Ultrafast all-optical switching in a silicon-nanocrystal-based silicon slot waveguide at telecom wavelengths," Nano Lett., 10, 1506-1511(2010).

[2] V. R. Almeida, C. A. Barrios, R. R. Panepucci and M. Lipson, "All-optical control of light on a silicon chip," Nature, 431, 1081-1084(2004).

[3] C. Koos, P. Vorreau, T. Vallaitis, P. Dumon, W. Bogaerts, R. Baets, B. Esembeson, I. Biaggio, T. Michinobu, F. Diederich, W. Freude and J. Leuthold, "All-optical high-speed signal processing with silicon-organic hybrid slot waveguides," Nat. Photonics, 3, 216-219 (2009).

[4] M. Hochberg, T. Baehr-Jones, G. Wang, M. Shearn, K. Harvard, J. Luo, B. Chen, Z. Shi, R. Lawson, P. Sullivan, A. K. Y. Jen, L. Dalton and A. Scherer, "Terahertz all-optical modulation in a silicon-polymer hybrid system," Nat. Mater., 5, 703-709(2006).

[5] J. I. Dadap, J. Shan, K. B. Eisenthal and T. F. Heinz, "Second-harmonic Rayleigh scattering from a sphere of centrosymmetric material," Phys. Rev. Lett. 83, 4045(1999).

[6] M. Kauranen and A. V. Zayats, "Nonlinear plasmonics," Nat. Photonics, 6, 737-748(2012).

[7] W. Cai, A. P. Vasudev and M. L. Brongersma, "Electrically controlled nonlinear generation of light with plasmonics," Science, 333, 1720-1723(2011).

[8] W. Wenseleers, F. Stellacci, T. Meyer-Friedrichsen, T. Mangel, C. A. Bauer, S. JK Pond, S. R. Marder and J. W. Perry, "Five orders-of-magnitude enhancement of two-photon absorption for dyes on silver nanoparticle fractal clusters," J. Phys. Chem. B, 106, 6853 -6863(2002).

[9] S. Palomba, M. Danckwerts and L. Novotny, "Nonlinear plasmonics with gold nanoparticle antennas," J. Opt. A: Pure Appl. Opt., 11, 114030(2009).

[10]M. Abb, P. Albella, J. Aizpurua, and O. L. Muskens, "All-optical control of a single plasmonic nanoantenna-ITO hybrid," Nano Lett., 11, 2457-2463(2011).

[11]C. Lu, X. Hu, Y. Zhang, Z. Li, H. Yang, and Q. Gong, "Large Nonlinearity enhancement of Ag/MEH-PPV nanocomposite by surface plasmon resonance at 1,550 nm," Plasmonics 7, 159-165(2012).

[12]H. B. Liao, R. F. Xiao, H. Wang, K. S. Wong and G. K. L. Wong, "Large third-order optical nonlinearity in Au: TiO_2 composite films measured on a femtosecond time scale," Appl. Phys. Lett., 72, 1817(1998).

[13]S. Chen, W. Wong, Y. Pun, K. Cheah and G. Li, "Surface plasmon-enhanced third harmonic generation from gold-polymer hybrid plasmonic crystal," Adv. Opt. Mater., 1, 522-526(2013).

[14]D. J. Ironside and J-T Shen, “Orders of magnitude enhancement of optical nonlinearity in subwavelength metal-nonlinear dielectric gratings,” Appl. Phys. Lett., 102, 021907(2013).

[15]G. A. Wurtz and A. V. Zayats, “Nonlinear surface plasmon polaritonic crystals,” Laser & Photon. Rev., 2, 125-135(2008).

[16]X. Yang, A. Ishikawa, X. Yin and X. Zhang, "Hybrid photonic-plasmonic crystal nanocavities," ACS Nano, 5, 2831-2838(2011).

[17]A. Scarpaci, A. Nantalaksakul, J. M. Hales, J. D. Matichak, S. Barlow, M. Rumi, J.W. Perry and S. R. Marder, “Effects of dendronization on the linear and third-order nonlinear optical properties of bis (thiopyrylium) polymethine dyes in solution and the solid state,” Chem. Mater., 24, 1606-1618(2012).

[18]Z. Li, Y. Liu, H. Kim, J. M. Hales, S. H. Jang, J. Luo, T. Baehr-Jones, M. Hochberg, S. R. Marder, J. W. Perry and A. K.-Y. Jen, “High-optical-quality blends of anionic polymethine salts and polycarbonate with enhanced third-order non-linearities for silicon-organic hybrid devices,” Adv. Mater., 24, OP326-OP330(2012).

[19]M. Grande, M. A.Vincenti, T. Stomeo, G. Morea, R. Marani, V. Marrocco, V. Petruzzelli, A. D’Orazio, R. Cingolani, M. De Vittorio, D. de Ceglia and M. Scalora, “Experimental demonstration of a novel bio-sensing

platform via plasmonic band gap formation in gold nano-patch arrays," Opt. Express, 19, 21385-21395(2011).

[20]B. D. Lucas, J.-S. Kim, C. Chin and L. Jay Guo, "Nanoimprint lithography based approach for the fabrication of large-area, uniformly oriented plasmonic arrays," Adv. Mater. 20, 1129-1134(2008).

[21] H. Raether, Surface Polaritons on Smooth and Rough Surfaces and on Gratings, Springer-Verlag, Berlin (1988).

[22]A. Christ, T. Zentgraf, J. Kuhl, S. G. Tikhodeev, N. A. Gippius and H. Giessen, "Optical properties of planar metallic photonic crystal structures: experiment and theory," Phys. Rev. B, 70, 125113(2004).

[23]B. Luk'yanchuk, N. I. Zheludev, S. A. Maier, N. J. Halas, P. Nordlander, H. Giessen and C. T. Chong, "the Fano resonance in plasmonic nanostructures and metamaterials," Nature Mater., 9, 707-715 (2010)

[24]R. M. Bakker, A. Boltasseva, Z. Liu, R. H. Pedersen, S. Gresillon, A. V. Kildishev, V. P. Drachev and V. M. Shalaev, "Near-field excitation of nanoantenna resonance," Opt. Express, 15, 13682-13688(2007).

[25]F. Ren, X. Wang and A. Wang, "Thermo-optic modulation of plasmonic bandgap on metallic photonic crystal slab," Appl. Phys. Lett., 102, 181101 (2013).

[26]R. Boyd, Nonlinear Optics, Ch. 2, Academic Press (1992).

[27]B. Corcoran, C. Monat, C. Grillet, D. J. Moss, B. J. Eggleton, T. P. White, L. O'Faolain and T. F. Krauss, “Green light emission in silicon through slow-light enhanced third-harmonic generation in photonic-crystal waveguides,” Nat. Photonics, 4, 206-210(2009).

CHAPTER 6. CONCLUSIONS

Optical interconnects have the fundamental advantages and are potential candidates for solving the bandwidth bottleneck problem. Appropriate devices, such as external optical modulators should be designed to meet the requirement of the systems.

This dissertation has dealt with the development of ultra-compact optical devices for surface-normal free-space modulation. The demand for bandwidth growth and high integration in advanced optical architecture has led us move the design from waveguides to free-space interconnection. Free-space optical interconnects have been proposed and studied for short-distance communications. The system architecture requires a high-speed, large-extinction-ratio, broadband-wavelength-range surface-normal modulator.

Surface-normal modulators using metallic photonic crystals were designed, fabricated, and experimentally tested. This active control of light intensity is achieved by engineering the Fano resonances in the metallic photonic crystals. Both thermo-optic and electro-optic modulation mechanisms were investigated, and the bandgap tuning due to those effects were demonstrated in Chapter 2 and Chapter 3. Further improvements of the electro-optic modulation performance will be focused on optimization of the poling process with more efficient and

thermally stable E-O polymers, and improving the FIB fabrication, which will lead to an ultra-compact device with fast modulation and low driving voltage.

Chapter 4 discusses the application of the hybrid plasmonic-organic structure for all optical switching processing devices. A material or device structure with large $\chi^{(3)}$ effect is desired for this application, therefore, we verify it by examining the third order harmonic generation. Over 20× enhancement factor with extraordinary third harmonic conversion efficiency was observed in the structure. Such device shows a route for future all optical signal processing devices.

A simple method to investigate the effect of finite grating size on RA-SPP resonances of plasmonic gratings was discussed in Chapter 5. The model could quickly and effectively predict the broadening of the transition edges of RA-SPP resonances, which agrees well with experimental results quantitatively.

In summary, our work towards the study of plasmonic bandgap modulation in metallic photonic crystals has led to compact devices to achieve out-of-plane optical interconnects. The modulation depth of these devices needs to be enhanced for better signal-to-noise ratio in interconnects. The limit of miniaturizing of the periodic structure also creates new challenges for the devices to further increasing the modulation depth due to the broadening of the bandgap edge. Such devices will need to be improved in the future work by designing a sharp transitional edge without losing the merit of compactness in plasmonic structures.